Neutrino emission characteristics of black hole formation in three-dimensional simulations of stellar collapse

Laurie Walk,[1] Irene Tamborra,[1] Hans-Thomas Janka[2], Alexander Summa,[2] and Daniel Kresse[2,3]

[1]*Niels Bohr International Academy and DARK, Niels Bohr Institute, University of Copenhagen, Blegdamsvej 17, 2100, Copenhagen, Denmark*
[2]*Max-Planck-Institut für Astrophysik, Karl-Schwarzschild-Str. 1, 85748 Garching, Germany*
[3]*Physik-Department, Technische Universität München, James-Franck-Straße 1, 85748 Garching, Germany*

Neutrinos are unique probes of core-collapse supernova dynamics, especially in the case of black hole (BH-)forming stellar collapses, where the electromagnetic emission may be faint or absent. By investigating two three-dimensional hydrodynamical simulations of BH-forming stellar collapses of mass 40 $M_\odot$ and 75 $M_\odot$, we identify the physical processes preceding BH formation through neutrinos and forecast the neutrino signal expected in the existing IceCube and Super-Kamiokande detectors, as well as in the future generation DUNE facility. Prior to the abrupt termination of the neutrino signal corresponding to BH formation, both models develop episodes of strong and long-lasting activity by the spiral standing accretion shock instability (SASI). We find that the spiral SASI peak in the Fourier power spectrum of the neutrino event rate will be distinguishable at 3σ above the detector noise for distances up to $\sim\mathcal{O}(30)$ kpc in the most optimistic scenario, with IceCube having the highest sensitivity. Interestingly, given the long duration of the spiral SASI episodes, the spectrograms of the expected neutrino event rate carry clear signs of the evolution of the spiral SASI frequency as a function of time, as the shock radius and postshock fluid velocity evolve. Because of the high accretion luminosity and its large-amplitude SASI-induced modulations, any contribution from asymmetric (dipolar or quadrupolar) neutrino emission associated with the lepton emission self-sustained asymmetry is far subdominant in the neutrino signal.

I. INTRODUCTION

Core-collapse supernovae (SNe) occur when stars with a zero-age main sequence mass roughly between $10 - 150\ M_\odot$ end their lives with the onset of gravitational collapse of their inner core [1–4]. The electron-degenerate iron core bounces and induces a shock wave in the infalling stellar mantle. As it travels outward, the shock wave loses energy by dissociating iron nuclei and stalls. According to the delayed SN mechanism, the SN then enters the accretion phase, in which infalling matter continually accretes onto the shock front [5]. In successful SNe, the shock wave is thought to be revived by neutrinos [6]. During the accretion phase, hydrodynamical instabilities such as the standing accretion shock instability (SASI), neutrino-driven convection, and the lepton emission self-sustained asymmetry (LESA) can develop, leading to large-scale asymmetries of mass distribution visible in the neutrino emission [7–14]. Convective overturn and SASI also enhance the rate of neutrino heating, aiding the revival of the SN explosion.

A revived SN explosion, in which the stellar mantle is successfully ejected, will result in the formation of a neutron star. However, a black hole (BH) will be the outcome if the explosion mechanism fails, and matter continues to accrete onto the transiently stable protoneutron star (PNS), pushing it over its mass limit. In 10%–30% of all core-collapse cases, or possibly more, the massive star is thus expected to end in a BH, as signified by the observation of disappearing red giants [15–18] and foreseen by recent theoretical work [19–21]. Since the BH is expected to form only after a period of postbounce accretion that continues for a few fractions of a second up to several seconds, the neutrino signal is expected to terminate abruptly [22]. Black hole–forming stellar collapses (sometimes also named "failed SNe") emit a faint electromagnetic signal originating from the stripping of the hydrogen envelope [23–25]. Sometimes, the BH formation may occur with a considerably longer delay, if not enough energy is released to finally unbind the star. In this case, a fraction of the stellar matter will fall back onto the PNS within minutes to hours, and the PNS will be pushed beyond its limit, leading to BH formation [3,26]. These so-called fallback SNe represent an intermediate class between ordinary SNe and BH-forming stellar collapses. The signals from fallback SNe will be similar to those of ordinary SNe with possible additional subluminous electromagnetic

displays [27]. Given the possibly dim or absent emission, BH-forming stellar collapses may be difficult to detect electromagnetically. Neutrinos (and possibly gravitational waves) can therefore be unique probes of these cataclysmic events. In this work, we will focus on the neutrino emission properties from BH-forming stellar collapses, where the BH formation occurs after few hundreds of milliseconds.

Early one-dimensional (1D) hydrodynamical simulations of BH-forming models in spherical symmetry were carried out in Refs. [19,20,28–31]. In Ref. [21], the effects of the nuclear equation of state (EoS), mass, metallicity, and rotation on BH formation were studied with a large set of so-called 1.5-dimensional progenitor models (i.e., employing spherical symmetry and an "approximate angle-averaged" rotation scheme). Recently, Ref. [32] investigated the time dependence of BH formation on the nuclear EoS in a 2D self-consistent simulation of a nonrotating 40 $M_\odot$ model. Together, these studies provide fundamental predictions of the key features of the neutrino emission properties from BH-forming models.

The detection of a neutrino burst from a nearby BH-forming stellar collapse is bound to yield precious hints about the BH formation; see, e.g., Refs. [33,34]. Moreover, the neutrino signal from BH-forming stellar collapses is of relevance in the context of the detection of the diffuse SN neutrino background; the detection of the latter will indeed provide insight on the fraction of BH-forming stellar collapses on cosmological scales [35–41].

The information carried by neutrinos from BH-forming stellar collapses has so far been explored using inputs from 1D hydrodynamical simulations only. In recent years, state-of-the-art three-dimensional (3D) simulations of core-collapse SNe with sophisticated energy-dependent neutrino transport have highlighted the plethora of information carried by neutrinos, especially for what concerns the preexplosion dynamics [14,42–56]. The first 3D simulation of BH formation and fallback was carried out in Refs. [57,58], motivated by the interest to explain astrophysical observations of metal-poor stars, natal kicks, and spins of BHs. It was found that the mass accretion rate remains large even directly after a possible shock revival. The rapid growth of the PNS can also cause a contraction of the postshock layer, which induces violent SASI activity [7,52,59], followed by the eventual collapse of the transient PNS into a BH [32,57,60].

This work aims to identify the dominant features in the observable neutrino signal characterizing BH formation. Our analysis is carried out with two 3D simulations of BH-forming stellar collapse with different progenitor masses and metallicities. The resulting neutrino emission properties are compared and contrasted to a set of simulations of ordinary nonrotating core-collapse SNe previously investigated by this group (specifically, we compare to a suite of 11.2, 15, 20, and 27 $M_\odot$ SN models; see Refs. [14,42,43,47,48]). By directly comparing to this set of models, the neutrino

properties which are unique to the postbounce evolution of a star collapsing to a BH are determined. We provide a first attempt to infer the underlying physical processes governing BH formation, using the features detectable through neutrinos with the IceCube Neutrino Telescope [61], Super-Kamiokande [62], and DUNE [63].

This paper is outlined as follows. In Sec. II, the key features of the BH-forming models used throughout this work are outlined. Section III discusses the neutrino emission properties, and how these properties relate to the SASI and LESA hydrodynamical instabilities is discussed in Secs. IV and V, respectively. The features detectable in the neutrino signal which are unique to BH formation are presented in Sec. VI. Finally, conclusions follow in Sec. VII.

II. SIMULATIONS OF BLACK HOLE FORMING STELLAR COLLAPSES

In this section, we briefly describe the key features of the two 3D hydrodynamical simulations used throughout this work. The neutrino emission properties will be described in the next section.

Two simulations of a nonrotating solar-metallicity ($Z_\odot \sim 0.0134$) 40 $M_\odot$ progenitor [64] and a metal-poor ($Z \sim 10^{-4} Z_\odot$) 75 $M_\odot$ star [4] were carried out with the PROMETHEUS-VERTEX code [65], which includes three neutrino flavors, energy-dependent ray-by-ray-plus neutrino transport, and state-of-the-art modeling of the microphysics [11,65–67]. Other codes employ multidimensional two-moment methods for the neutrino transport; see, e.g., Refs. [68–70]. In Ref. [69], 3D core-collapse simulations of a nonexploding 20 $M_\odot$ model and an exploding 9 $M_\odot$ model were compared with ray-by-ray-plus transport approximation and multidimensional transport. No major differences with respect to the hydrodynamic evolution and the basic features of the neutrino emission (luminosities and mean energies as functions of time) could be found beyond the small-scale (in space and time) fluctuations that are characteristic of the ray-by-ray method and variations in the nonlinear dynamics that generically exhibit stochasticity and can be triggered by any kind of differences between simulations (e.g., a trivial phase shift of large-amplitude SASI shock oscillations in the 20 $M_\odot$ model). Naturally, however, from these two representative models, it cannot be concluded that cases do not exist where method-specific transport effects can be more relevant, for example, in the collapse of rapidly rotating stellar cores, where the global deformation of the protoneutron star sets limitations to the applicability of the ray-by-ray approximation. Both of our simulations were performed on an axis-free Yin-Yang grid [71,72].

In hydrodynamical simulations of BH-forming models, where the central density and mass of the PNS continue to grow to relatively large values, an implementation of general relativity (GR) is crucial. The VERTEX code

approximates the effects of GR by replacing the Newtonian gravitational potential with a modified Tolman-Oppenheimer-Volkoff (TOV) potential, as proposed in Refs. [65,73] and implemented in Refs. [32,34,60, 74–77]. Specifically, by prescribing the TOV potential according to Case A in Ref. [73], the full GR results can be closely reproduced, while keeping a sophisticated treatment of neutrino transport and the simulation costs lower than needed for solutions of the Einstein field equations. In particular, the use of the TOV potential allows for the reproduction of the duration of the time interval of accretion until BH formation and the corresponding neutrino energy release found in full GR 1D simulations fairly accurately [34,74,78]. However, by adopting the approximate treatment of GR proposed in Ref. [73], we have no way to recognize the formation of the event horizon, but we diagnose the onset of BH formation simply by a rapid rise of the central density and a corresponding drop of the lapse function. Redshift corrections and time dilation are included in the neutrino transport, while relativistic transformations of the spatial coordinates are excluded in order to remain consistent with the Newtonian hydrodynamics equations governing the fluid dynamics in these simulations [65].

The simulation of the 40 $M_\odot$ SN model has an angular resolution of 5 deg and a temporal resolution in the data output of 0.5 ms. The simulation of the 75 $M_\odot$ SN model was run with the newly implemented static mesh refinement grid [79]; i.e., the neutrino transport was computed on a 2 deg grid, but the hydrodynamic evolution was computed on a grid refined radially outward up to 0.5 deg (doubling the angular resolution roughly at the position of the gain radius and at a fixed radius of 160 km). The adopted temporal resolution of the 75 $M_\odot$ model is of about 0.2 ms in the data output. We stress that our angular resolution may not be completely satisfactory with respect to obtaining full convergence [79–81]; however, we accept this compromise for being able to choose high radial resolution with initially 400 radial zones, being nonequidistantly distributed from the center to an outer boundary at 10^4 km with an inflow condition, and continuous refinement up to 650 radial zones toward the time when the simulations were stopped. Moreover, a comparison of the 75 $M_\odot$ model with a low-resolution run of 5 deg reveals essentially no differences in the dynamical evolution and neutrino emission (the main difference being a 4 ms earlier approach to BH formation in the low-resolution case); for this reason, we discuss only the better resolved case here.

The simulation of the 40 $M_\odot$ SN model employed the nuclear EoS of Lattimer and Swesty [82] with nuclear incomprehensibility of 220 MeV. The collapse into a BH occurs at ∼570 ms postbounce. The simulation of the 75 $M_\odot$ SN model again used the Lattimer and Swesty EoS, and the BH formation occurs at ≃250 ms postbounce, indicating a higher accretion rate and therefore a shorter accretion phase compared to the 40 $M_\odot$ model. Admittedly, the Lattimer and Swesty EoS adopted for both models is not consistent with all laboratory constraints of high-density nuclear matter [83]. More modern EoSs, for example those discussed in Ref. [84], may yield a different maximum neutron star (NS) mass and therefore duration of postbounce accretion until BH formation. Nevertheless, we do not expect our general results and generic effects to be much affected by the shortcomings of the employed EoS. Accordingly, for example, a 5 deg 3D simulation of the 75 $M_\odot$ progenitor with the Steiner-Fischer-Hempel (SFHo) EoS [84] exhibits a shock history very similar to the 75 $M_\odot$ run with the Lattimer and Swesty EoS, but BH formation occurs only after 325 ms, and a 75 $M_\odot$ simulation with a resolution of 5 deg with the DD2 EoS [84] shows a dynamical evolution very close to the 40 $M_\odot$ model with the Lattimer and Swesty EoS until BH formation at 519 ms after bounce. The results will be presented in detail in another work, and we focus here on two representative cases to explore the imprints of BH formation carried by neutrinos.

Figure 1 displays the time evolution of the characteristic quantities for the two models. The 75 $M_\odot$ model settles to a generally constant mass accretion rate after the infall of the Si/O interface through the shock (top panel) and a steep increase in the baryon density (third panel) in the instants preceding the BH formation. Because of stabilizing effects of thermal pressure, BH formation sets in when a mass has been accreted onto the transiently stable PNS that is higher than the maximum mass of cold NSs for the employed EoS [78], which allows a maximum baryonic mass of about 2.3 $M_\odot$ [84]. In both models, the PNS baryonic mass, plotted in the second panel of Fig. 1, rapidly increases and reaches a value of around 2.5 $M_\odot$ just before the BH formation.

As can be seen in the plot of the shock radius evolution (fourth panel), shock expansion occurs in the 75 $M_\odot$ model just prior to the BH formation, similarly to what was observed in Refs. [32,57,60]. On the other hand, this does not happen for the 40 $M_\odot$ model where the average shock radius reaches a quasistationary value, although with considerable excursions with time. This trend in the shock radius for the 40 $M_\odot$ model differs from that of the 40 $M_\odot$ model simulated in two dimensions with the same EoS and nuclear incompressibility in Ref. [32]. In fact, the latter showed a shock revival prior to the collapse of the PNS into a BH. Similarly, the simulation of a 40 $M_\odot$ model considered in Ref. [56], albeit with a different EoS, exhibits a shock expansion at a postbounce time of ≃200 ms. Figure 1 also shows that, in our 40 $M_\odot$ model, episodes of shock contraction and expansion occur just before the BH formation, while in our 75 $M_\odot$ model, the shock radius quickly expands before the PNS collapses into a BH. As expected and shown in the bottom panel of Fig. 1, the PNS radius rapidly contracts until the BH forms.
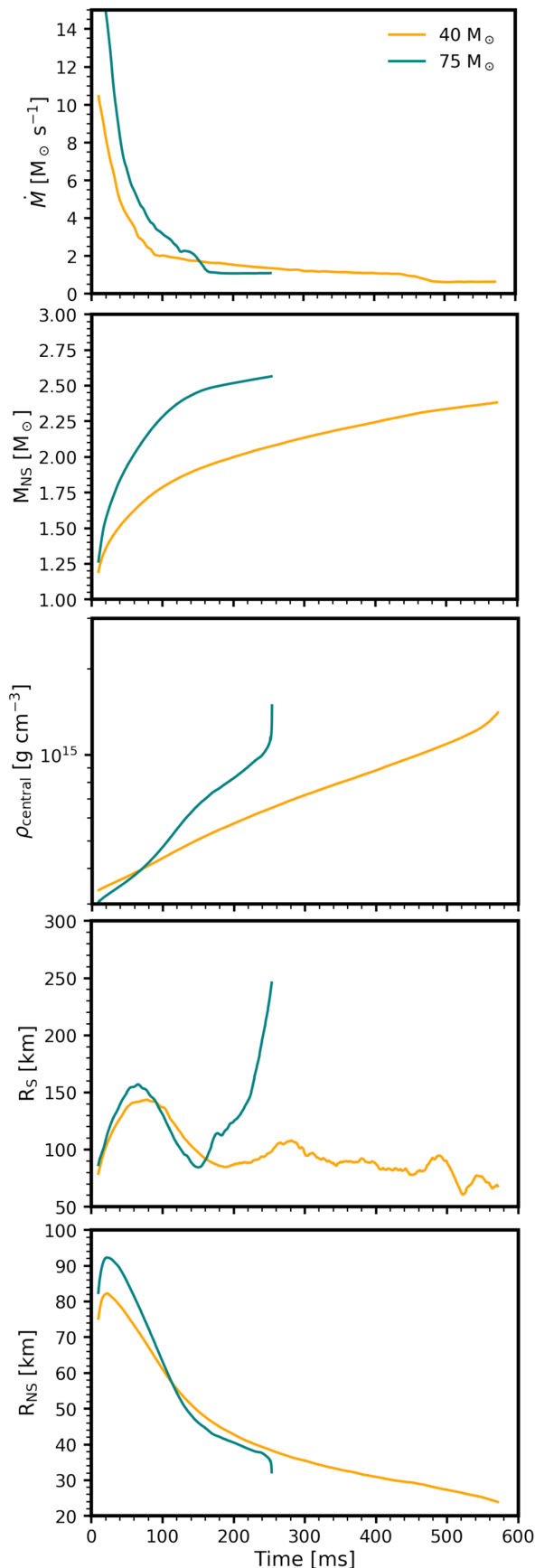
FIG. 1. (Continued)

III. NEUTRINO EMISSION PROPERTIES

The neutrino signal carries unique imprints of the hydrodynamical instabilities governing the accretion phase. To determine those characteristics of the onset of BH formation, we explore the evolution of the emitted neutrino properties of our 40 $M_\odot$ and 75 $M_\odot$ models. The neutrino properties were extracted at a radius of 500 km and remapped from the Yin-Yang simulation grid onto a standard spherical grid. The neutrino emission properties for each flavor have been projected and plotted to appear as they would for a distant observer located along a specific angular direction, following the procedure outlined in Appendix A of Ref. [42] and in Ref. [85]. We emphasize that the observer projections are a postprocessing measure intended to help overcome the shortcomings of the ray-by-ray transport (i.e., the fact that the ray-by-ray approximation considers only radial fluxes, whereas distant observers receive neutrinos from all locations on the hemisphere facing the observer). As a consequence, small local variations in the neutrino emission properties connected to the ray-by-ray transport approximation will be hemispherically averaged out through the observer projections. The neutrino emission properties for every angular direction, as well as the 4π-equivalent ones, can be provided upon request for both models.

A. Directionally independent neutrino emission properties

Before investigating the directional dependence of the neutrino emission properties, we focus on characterizing the global features of the 40 $M_\odot$ and 75 $M_\odot$ models that may be unique to BH-forming stellar collapses. We do this by considering the neutrino emission properties obtained after integrating over all observer directions.

Both of our models develop long-lasting phases of SASI activity. Spiral SASI motions of the postshock layer partly continue for periods of more than 100 ms and can change their direction and main plane of the spiral motions.

FIG. 1.   Evolution of the preshock mass accretion rate (at 400 km), NS baryonic mass, baryonic density at the NS center, spherically averaged shock radius, and NS radius (defined at a density of 10^{11} g cm^{-3}) for the 40 $M_\odot$ (in orange) and 75 $M_\odot$ (in teal) models, from top to bottom. All curves have been smoothed with running averages over intervals of 5 ms. The 40 $M_\odot$ model forms a BH at a postbounce time of about 570 ms, while the 75 $M_\odot$ model undergoes a more rapid evolution and forms a BH at a postbounce time of roughly 250 ms. Shock expansion occurs in the 75 $M_\odot$ model in the phase preceding the BH formation as the central density steeply increases; see also Ref. [56]. The shock radius exhibits a generally stationary value with slow evolution in the 40 $M_\odot$ model. The 40 $M_\odot$ model shows episodes of shock contraction and expansion just before the BH formation. In both models, the NS baryonic mass rapidly increases, reaching a value of about 2.5 $M_\odot$ before the BH formation.

In addition, there are also short episodes of SASI dipolar and quadrupolar sloshing activity that precede the SASI spiral phases and bridge phases where the spiral motions possess different direction vectors.

The top panels of Fig. 2 show the luminosity of each neutrino flavor (ν_e, $\bar{\nu}_e$, and $\nu_x = \bar{\nu}_x = \nu_\mu$, ν_τ) extracted at 500 km and individually obtained by integrating over all observer directions for both models. The red, blue, and green curves refer to ν_e, $\bar{\nu}_e$, and ν_x, respectively. One can see that the large amplitude modulations due to spiral SASI [8,86,87] survive in the 40 $M_\odot$ model (left panel), even after averaging over all observer directions, suggesting that spiral SASI is quite strong in this model. This is in agreement with the findings of Ref. [88], which also found strong spiral SASI activity in the context of compact shocks. On the contrary, this is not the case for the 75 $M_\odot$ model (right panel). Moreover, the 75 $M_\odot$ model has a shorter accretion phase prior to BH formation and a higher overall neutrino luminosity.

Comparing the global neutrino properties of these models with the ones of ordinary SNe, see, e.g., the neutrino properties of the SN models presented in

Refs. [42,47,48] simulated with the same neutrino transport and nuclear EoS and the large suite of models in Ref. [88], we find that the neutrino luminosity is higher for the BH-forming models, up to a factor of 2 for the 75 $M_\odot$ model. The neutrino signal terminates at 572 and 250 ms for the 40 $M_\odot$ and 75 $M_\odot$ models, respectively, corresponding to BH formation [22]. After ~140–160 ms postbounce, the ν_e luminosity—and after ~100 ms the ν_x luminosity—drop moderately in the 40 $M_\odot$ model because of the constant mass accretion rate but rapid PNS contraction (see top and bottom panels of Fig. 1). This decline is on a minor scale compared to the effect of the Si/O shell interface on the neutrino luminosity in the 40 $M_\odot$ model at around 440–480 ms, and it happens more gradually over a longer period of time from about 100 to 220 ms. Since the mass accretion rate ahead of the shock, during this time interval of the luminosity decline, is nearly constant and the average shock even retreats (enhancing the PNS accretion until ~190 ms), we have no other explanation for this phenomenon than the ongoing, rather pronounced, contraction of the PNS, leading to a decrease of the neutrinospheric radius. After ~190 ms postbounce, shock expansion sets in and
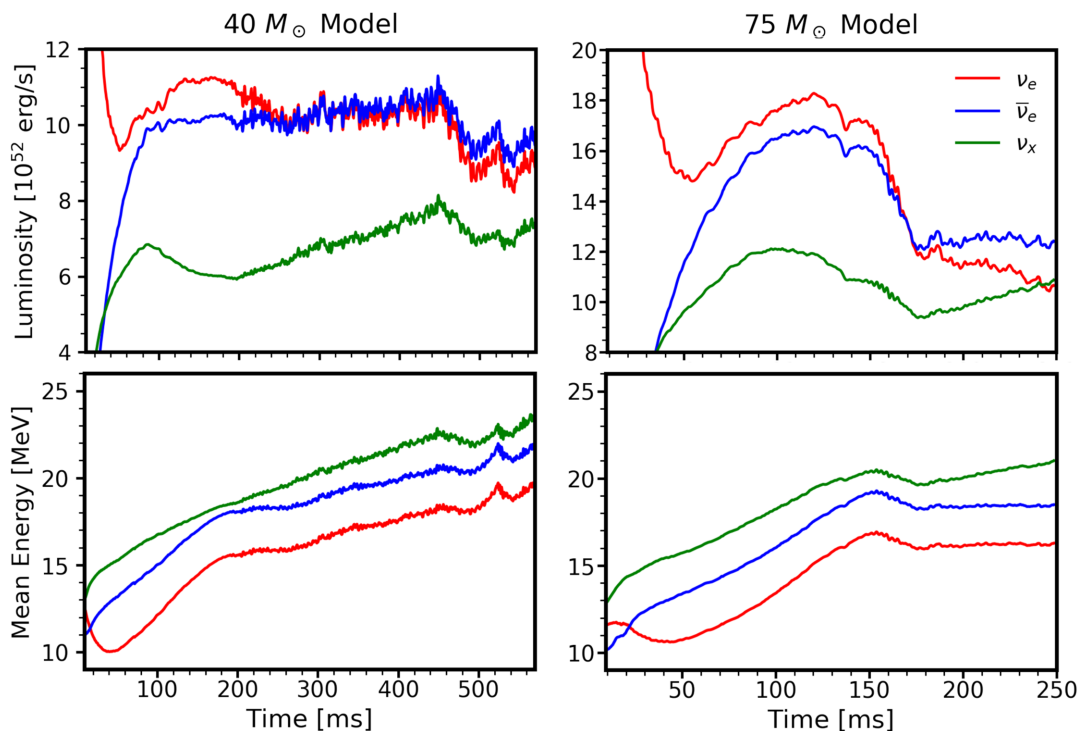

FIG. 2. *Top panels:* Luminosity of each neutrino flavor (ν_e, $\bar{\nu}_e$, and ν_x in red, blue, and green, respectively) for the 40 $M_\odot$ (left) and 75 $M_\odot$ (right) models after integrating over all observer directions. The luminosity for the 40 $M_\odot$ model drops at ~450 ms corresponding to the infall of the Si/O interface and at ~510 ms, tracking the shock contraction and expansion just before the BH formation. Notably, SASI modulations in the neutrino luminosity are still clearly visible in the 40 $M_\odot$ model, hinting toward very strong SASI activity. A steady increase in the ν_x luminosity is observed for both models in more or less the same temporal interval where SASI occurs. Additionally, a crossing between the ν_e and $\bar{\nu}_e$ luminosities can be seen, just before the onset of BH formation. *Bottom panels:* Mean energies (i.e., energy flux divided by number flux) of each neutrino flavor as a function of time. As opposed to the luminosity, the average energies show the same hierarchy throughout the whole signals duration. The luminosities and mean energies have been evaluated at a radius of 500 km.

supports the decline of the ν_e luminosity by reducing PNS accretion. After about 260–270 ms postbounce, a transient phase of slowly rising luminosities of all neutrino species follows. At ∼450 ms postbounce, the infall of the Si/O interface in the 40 $M_\odot$ model leads to another temporary decline in the neutrino luminosity and to shock expansion. Notably, the neutrino luminosity increases after this drop, until ∼510 ms, when it drops again. After this second drop, the luminosity climbs until the onset of the collapse to a BH. This late behavior tracks the contraction and expansion of the shock radius observed in Fig. 1. Around ∼550 ms, the shock radius contracts again (see the fourth panel of Fig. 1), leading to an increase in the luminosity and finally to the onset of BH formation.

Another notable feature, present in both BH-forming models, is the steady increase in the ν_x luminosity in [150, 400] ms for the 40 $M_\odot$ model and after the drop due to the crossing of the Si/O interface at 175 ms for the 75 $M_\odot$ model. This trend in the ν_x luminosity is characteristic of BH-forming models with a high-mass accretion rate. It may be explained by a significant increase in temperature as the PNS contracts, similar to what was found in Ref. [28]. The higher temperatures lead to an increased production of μ and τ neutrinos. Moreover, a crossing between the ν_e and $\bar{\nu}_e$

luminosities occurs. In fact, the ν_e luminosity tends to steadily drop after the crossing of the Si/O interface at 450 ms (175 ms) for the 40 $M_\odot$ (75 $M_\odot$), while the $\bar{\nu}_e$ luminosity stays almost stationary. This decrease of the ν_e luminosity is more pronounced in the simulation of the 75 $M_\odot$ model, which also has a more massive and more rapidly contracting PNS, suggesting a possible connection between the two. Although the crossings of the electron neutrino and antineutrino luminosities are an interesting feature appearing in these models, they are not in the focus of our present discussion; additional analysis and more models with different EoSs are needed in one, two, and three dimensions to clarify the exact origin of these crossings and to reveal whether they are generic to BH formation in 3D. The mean energies in the lower panels of Fig. 2 are calculated by dividing the energy flux by the number flux. No crossing of the mean energies of $\bar{\nu}_e$ and ν_x occurs, in contrast to what was found in core-collapse simulations with lower-mass accretion rates and correspondingly less rapidly growing PNS masses (see, e.g., Ref. [89]). Notably, the rise of the mean energy of ν_x is milder in these models than observed in 1D simulations of BH-forming stellar collapses by other groups [30,31] because of the inclusion of energy transfer in neutrino-nucleon scattering reactions
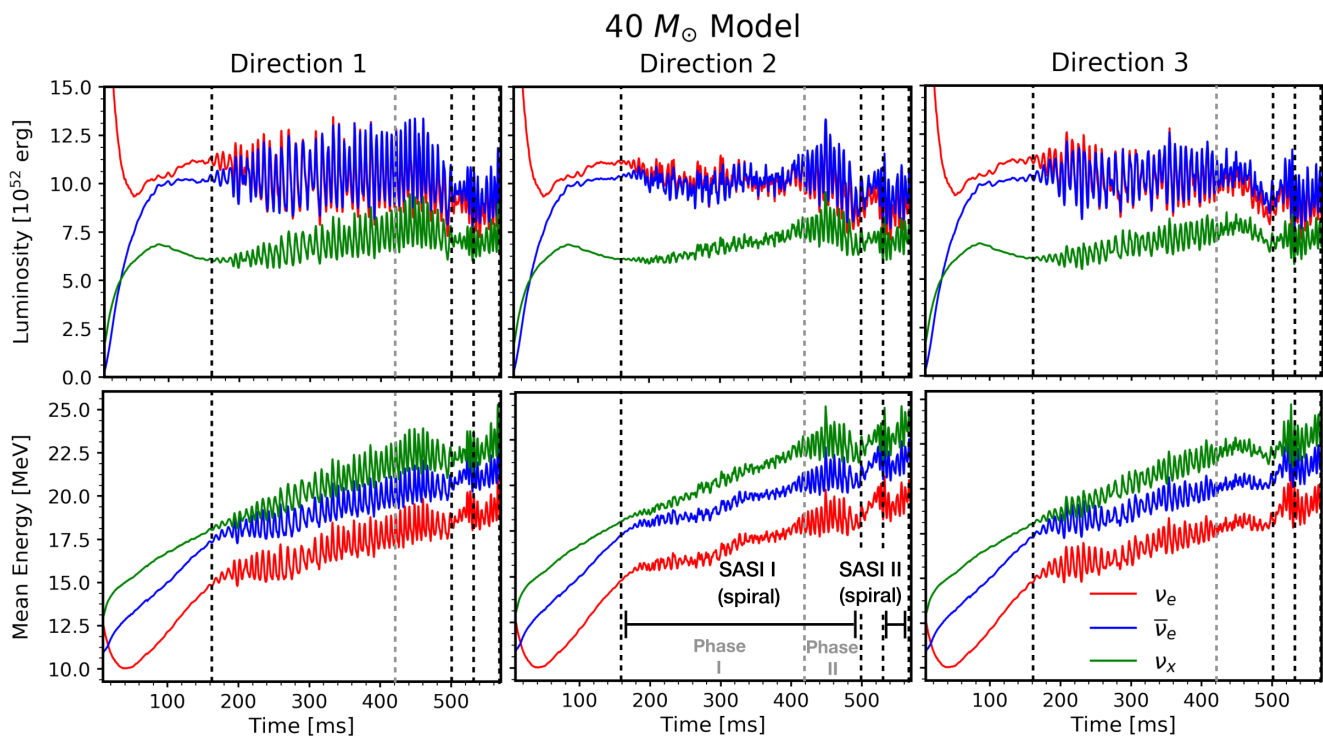

FIG. 3. Luminosities (top) and mean energies (bottom) of ν_e, $\bar{\nu}_e$ and ν_x (red, blue, and green, respectively), along three observer directions for the 40 $M_\odot$ model as functions of postbounce time. The motivation for selecting the three observed directions shown in this plot will be discussed in Sec. IV, see also Fig. 6. A long-lasting spiral SASI phase (SASI I) is identified along Direction 1 (left panel) in [160, 500] ms, as indicated by the black dashed vertical lines. By comparing the neutrino signal along Directions 1 and 2, this interval can be divided into two sub-intervals, [160, 420] ms and [420, 500] ms, divided by the grey dashed line. In fact, the SASI plane evolves over time, shifting its orientation at ∼420 ms. Modulations corresponding to a second spiral SASI episode (SASI II) are visible in the interval [530, 570] ms. The spiral nature of the SASI episodes is further investigated in Sec. IV.

in the neutrino transport of our models (for the correspondingly similar behavior in 1D models, see Ref. [34]).

B. Directionally dependent neutrino emission properties

Previous work [42–48,51,54,88,90] pointed out that the neutrino emission properties are highly directionally dependent. More specifically, in SN models showing SASI activity, sinusoidal modulations in the neutrino signal are associated with periodic deformations of the shock wave. In the case of sloshing or spiral SASI, such modulations are expected to be visible to an observer along the SASI direction or SASI plane, while they may nearly disappear for an observer located perpendicular to the SASI plane [42,43,88]. Building on these findings, we attempt to identify potential SASI episode(s) in the BH-forming models by looking for modulations in the neutrino signal and scanning over all observer directions.

Figure 3 shows the neutrino luminosities and mean energies for the 40 $M_\odot$ model as a function of the postbounce time along three selected observer directions.

The three directions are specifically chosen to highlight the most extreme modulation amplitudes of the neutrino signal and to show the maximal variation between periods of modulation. The precise choice of the location of the three selected directions relative to the orientation of the spiral SASI dipole will be discussed in Sec. IV.

Along direction 1, a period of high amplitude modulation of the neutrino properties can be observed in the interval [160, 500] ms. These modulations are indicative of a single long spiral SASI phase along the plane of observation (SASI I). By comparing the left and central panels of Fig. 3, however, one can see that only the modulations in [160, 420] ms decrease upon changing to an observer along direction 2 (SASI I, phase I). The modulations in the second subinterval, [420, 500] ms, disappear by shifting to an observer placed along direction 3 (SASI I, phase II). This suggests a change of the main spiral SASI plane at the interval [420, 500] ms. Whether the shift of the spiral SASI plane occurs gradually or instantaneously cannot be easily inferred by scanning through the observer directions alone and will be further investigated in
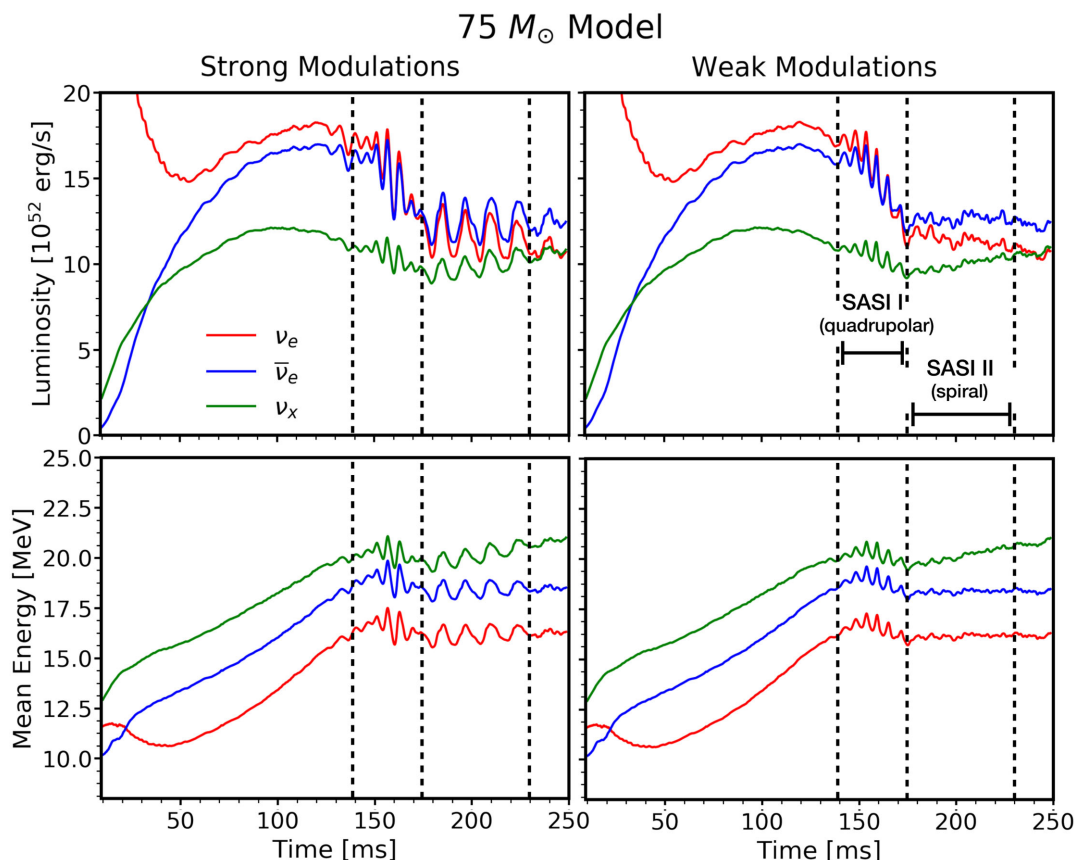

FIG. 4.   Analogous to Fig. 3, but for the 75 $M_\odot$ model. For this model, only two directions, the one of strongest (left) and weakest (right) overall signal modulation, are displayed to identify the spiral SASI phases, as will be further discussed in Sec. IV. The coordinates of the observer corresponding to these two directions are given in the lower two panels in Fig. 6. A quadrupolar moment dominates the neutrino emission between [140, 175] ms. This is followed by dipolar modulations of the neutrino emission due to spiral SASI in [175, 230] ms. Note that the quadrupolar modulations are due to a quadrupolar SASI mode and do not depend strongly on the direction. Similar to the 40 $M_\odot$ model, the second SASI episode has a spiral nature, which is investigated in Sec. IV.

the next section. Finally, a second period of signal modulation can be identified in Fig. 3 between [530, 570] ms (SASI II). This indicates the occurrence of a second spiral SASI episode for the 40 $M_\odot$ model, which develops directly after the infall of the Si/O interface, and appears to remain stable until the collapse into a BH.

Similarly, Fig. 4 shows the neutrino properties of each flavor for the 75 $M_\odot$ model. Upon scanning over all observer directions, two directions are extracted to illustrate the behavior of this model; a direction of "weak modulations," in which there is minimal total variation of the signal compared to the average variation, and a direction of "strong modulations," where the amount of signal variation is maximal. A first phase of signal modulations is apparent in the interval between [140, 175] ms. These modulations remain present in the signal throughout all scanned observer directions and are due to SASI quadrupolar sloshing motions, as will be evidenced and investigated in the next section. Following this, a spiral SASI phase can be identified in the interval of [175, 230] ms. As expected,

the latter depends more strongly on the observer direction, thus disappearing when shifting between the directions of strong and weak modulations.

For both models, we find that the SASI modulations affecting the neutrino signal are stronger for ν_e and $\bar{\nu}_e$ than for ν_x. Similar results were also found in Refs. [42,48,88].

IV. CHARACTERIZATION OF SASI IN BLACK HOLE–FORMING MODELS

To obtain a better characterization of SASI in the BH-forming models, and to verify the conjectures of the SASI episodes presented in the previous section, a detailed investigation of the temporal evolution of SASI is required. This is the focus of this section.

The full animation of the time evolution of the $\bar{\nu}_e$ luminosity relative to its 4π average, $[(L_{\bar{\nu}_e} - \langle L_{\bar{\nu}_e}\rangle)/\langle L_{\bar{\nu}_e}\rangle]$ for the 40 $M_\odot$ model, provided as Supplemental Material [91] of this paper, reflects that spiral SASI activity dominates the dynamics of this model. The development of a SASI
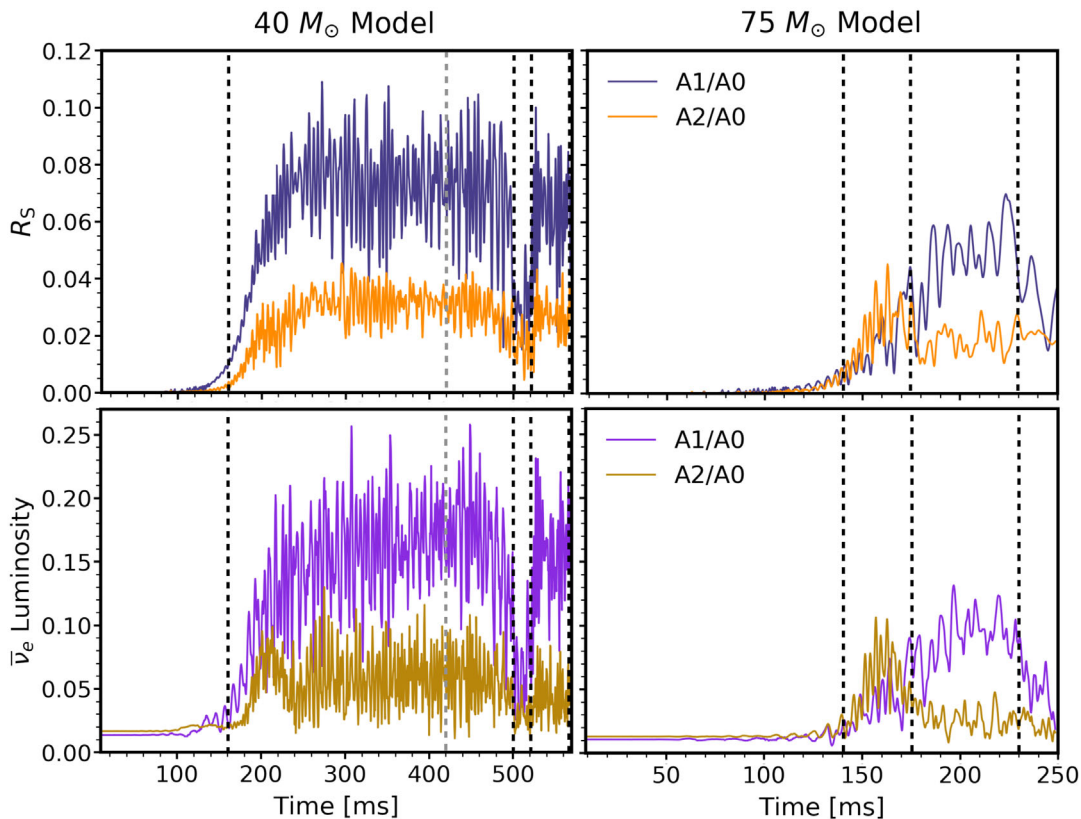

FIG. 5. Time evolution of the strength of the dipole (purple) and quadrupole (gold) moments of the shock surface (top) and $\bar{\nu}_e$ luminosity (bottom), each normalized to its monopole for the 40 $M_\odot$ (left) and 75 $M_\odot$ (right) BH-forming models. The dashed vertical lines mark the spiral SASI intervals for each model (see Sec. III B). SASI dipole and quadrupole modes of the shock surface correlate tightly with the ones of the neutrino-emission asymmetries. The luminosity dipole dominates for both models throughout the spiral SASI phases. For the 75 $M_\odot$ model, the quadrupole moment dominates in the interval [140, 175] ms, confirming that the signal modulations observed in Fig. 4 (SASI I) are due to a quadrupolar mode in the neutrino emission. The transition of a dominant quadrupolar ($l = 2$) to a dominant dipolar ($l = 1$) neutrino emission mode is a consequence of the rapid expansion of the shock radius caused by a drop in the mass accretion rate.

spiral mode has been previously found in 3D hydrodynamical simulations; see, e.g., Refs. [8,13,88,92–95].

SASI motions of the postshock layer modulate the accretion flow onto the PNS and thus lead to large-amplitude variations of the accretion luminosity [42,88]. As a consequence, a dominant dipole in the shock surface has been shown to be correlated with dominant dipole in the neutrino luminosity; e.g., see Fig. 3 of Ref. [92], Fig. 8 of Ref. [48], Fig. 13 of Ref. [94], and Fig. 18 of Ref. [88]. Building on these findings and following the approach introduced in Sec. IV of Ref. [48], we employ a multipole analysis of the shock surface and of the neutrino luminosity and track the evolution of the multipoles in time. For simplicity, we limit our analysis to the $\bar{\nu}_e$ signal; however, similar trends are found for the other (anti)neutrino species.

We estimate the monopole (A_0), dipole (A_1), and quadrupole (A_2) as described in Sec. IV and Eq. (5) of Ref. [48]. Figure 5 shows that the spiral SASI dipole and sloshing

quadrupole modes dominate in different phases and correlate tightly with the dominance of dipole or quadrupole neutrino-emission asymmetries. The left panels of Fig. 5 show the time evolution of A_1 and A_2 relative to A_0 for the $\bar{\nu}_e$ luminosity and the shock surface of the 40 $M_\odot$ BH-forming model. The dashed vertical lines indicate the two spiral SASI intervals described in Sec. III B (SASI I and SASI II). In both intervals, the dipole moment is dominant, confirming the development of spiral SASI in each time window, compatibly with what was discussed in Refs. [48,88].

To investigate the shift of the spiral SASI plane at ∼420 ms during the SASI I episode, the direction of the positive neutrino dipole moment is tracked along the SN emission surface over time in the top panels of Fig. 6. The left and central panels show the first spiral SASI episode split up into the two subtime intervals identified in Fig. 3 (SASI I, phases I and II), and the right panel shows the
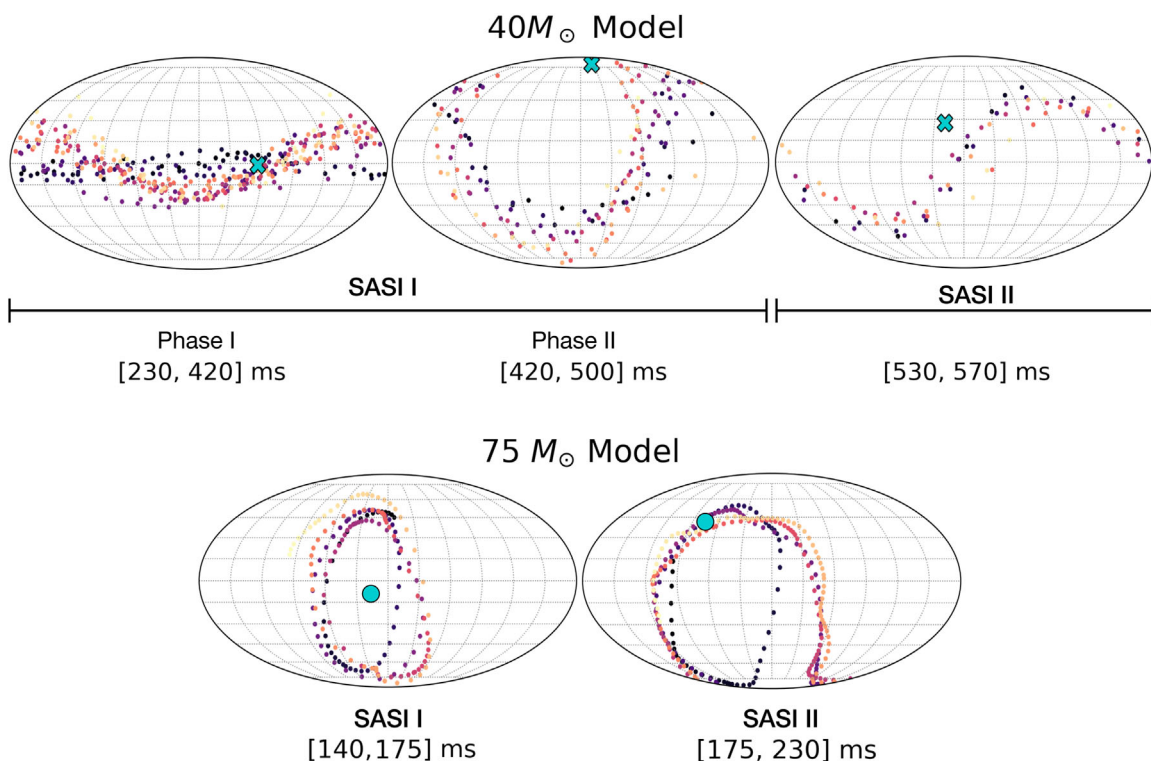

FIG. 6. Time evolution of the direction of the $\bar{\nu}_e$ luminosity dipole moment for the different SASI time intervals identified in Sec. III B for the 40 $M_\odot$ (top) and the 75 $M_\odot$ (bottom) models. The dots mark the path of the positive luminosity dipole direction, and the color hues become lighter as time increases. *Top, left*: The (SASI I, phase I) episode has been shortened and plotted only in [230, 420] ms to highlight its trend more clearly, as the luminosity dipole is less stable at earlier times. In this time interval, spiral SASI motions develop roughly along the equatorial plane (see also Fig. 7). The cyan marker indicates the coordinates of an observer along direction 1; see left column of Fig. 3. *Top, middle*: Same as the left panel but for [420, 500] ms (SASI I, phase II). The cyan marker indicates the coordinates of an observer along direction 2 (see Fig. 3). Between postbounce times of approximately 380–420 ms, the SASI plane shifts to a plane almost perpendicular to the equator. *Top, right*: Track of the $\bar{\nu}_e$ luminosity dipole moment over the second spiral SASI episode (SASI II). The marker indicates the coordinates of an observer along direction 3. *Bottom*: Time evolution of the $\bar{\nu}_e$ luminosity dipole direction of the 75 $M_\odot$ model in the first ([140, 175] ms, left) and second ([175, 230] ms, right) SASI intervals (SASI I and SASI II, respectively; see Fig. 7). The markers indicate the coordinates of an observer along the strong modulations direction (right) and the weak modulations direction (left); see Fig. 4. In this model, the luminosity dipole follows a stable and quite narrow path.

second spiral SASI episode (SASI II). The circular paths of the $\bar{\nu}_e$ dipole moment over the emission surface visible in Fig. 6 suggest the spiral nature of SASI in this model. To further highlight the spiral character of both spiral SASI episodes, the left panel of Fig. 7 shows the $\bar{\nu}_e$ luminosity dipole evolution projected onto a 3D spherical map for short, representative time intervals.

From Fig. 6, it is clear that the first spiral SASI phase kicks in along the equatorial plane. Here, it remains relatively stable until ~420 ms. After that, the spiral SASI plane morphs from an equatorial one to the almost perpendicular plane spun by the circular pattern in the central panel of Fig. 6 (see also Fig. 7). Direction 1 (marked in the top left panel of Fig. 6) lies on both the equatorial plane and this shifted plane, explaining the presence of signal modulations over the full interval, [160, 500] ms, in the left panel of Fig. 3. Direction 2 (see top middle panel of Fig. 6), however, lies far away from the equator, and thus the central panel of Fig. 3 does not show strong amplitude modulations in the first subtime interval. The marker of direction 3 (top right panel of Fig. 6) lies away from the plane to which the second phase of the first spiral SASI episode evolves in the interval [420, 500] ms (SASI II), and thus the signal modulations in this interval shrink considerably between direction 2 and direction 3 in Fig. 3. The markers in Fig. 6 indicate the coordinates along which directions 1, 2, and 3 in Fig. 3 lie, from left to right, respectively. When scanning over all observer directions, these directions were chosen because the total modulations along each of them differ maximally compared to the modulations visible in the other two directions.

The evolution of the spiral SASI plane over time is special for this BH-forming model and may be observable due to the long duration of the first spiral SASI episode. SASI spiral modes are thought to develop as a result of a superposition of two SASI dipolar modes oscillating out of phase with each other along different directions [8,13,88,92]. The shift of the plane of the SASI spiral mode observed in this model may be caused by the presence of a second, subdominant SASI mode along a different direction or by a stochastic fluctuation. However, to fully understand the physical origin of the shift in the spiral SASI plane, one must consider the full range of hydrodynamical properties of this model. Such an investigation lies beyond the scope of this work, in which the neutrino emission properties are the main focus.

The right panels of Fig. 5 show the corresponding relative dipole and quadrupole strengths of the $\bar{\nu}_e$ luminosity for the 75 $M_\odot$ model as functions of time. Interestingly, in the right panels of Fig. 5b the quadrupole moment dominates in the earlier interval, [140, 175] ms, confirming that the corresponding SASI modulations identified in the neutrino luminosity have a quadrupolar sloshing nature. This quadrupolar emission pattern correlates with a dominant quadrupolar sloshing mode of SASI mass motions of the postshock layer as demonstrated by our spherical harmonics decomposition of the shock surface. In fact, by plotting the $\bar{\nu}_e$ luminosity relative to its 4π average ($\langle L_{\bar{\nu}_e} \rangle$) on a Molleweide map for the SN emission surface at four consecutive snapshots in time in Fig. 8, a clear quadrupolar pattern of SASI can be seen. The SASI quadrupolar sloshing activity is even more apparent in the
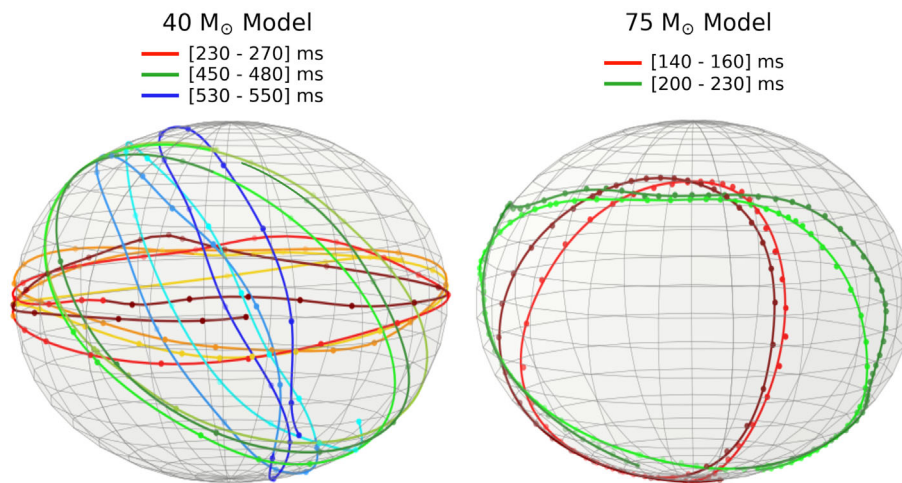

FIG. 7. Time evolution of the direction of the $\bar{\nu}_e$ luminosity dipole moment (see Figs. 5 and 6) onto a 3D spherical map for selected short time intervals for the 40 $M_\odot$ (left) and the 75 $M_\odot$ (right) models. The red, green, and blue color codes represent different time intervals during the spiral SASI episodes of each model. Each individual full cycle of SASI is plotted with a different shade of color to indicate the time evolution. The dots mark the time evolution corresponding to the temporal grid of the simulation output. The circular paths of the neutrino luminosity dipole clearly indicate the spiral nature of the SASI episodes in the 40 $M_\odot$ model. Similar conclusions hold for the second selected time interval (green) of the 75 $M_\odot$ model. During the earlier quadrupolar sloshing SASI phase of the 75 $M_\odot$ model (red), the dipole evolves along a 90° slice in one hemisphere, while the quadrupolar moment dominates the neutrino emission (see also Fig. 5).

full animation of the $\bar{\nu}_e$ luminosity relative the 4π average, added as Supplemental Material [91] of this paper, from which the snapshots in Fig. 8 have been taken.

Once the Si/O shell interface has fallen into the shock front at ∼175 ms, the shock front expands, increasing the volume within the gain layer (see Fig. 1). This leads to favorable conditions for the development of a dipolar SASI mode [96] and thus of spiral SASI activity in the 75 $M_\odot$ model as shown in the right panels of Figs. 5 and 7, and it is
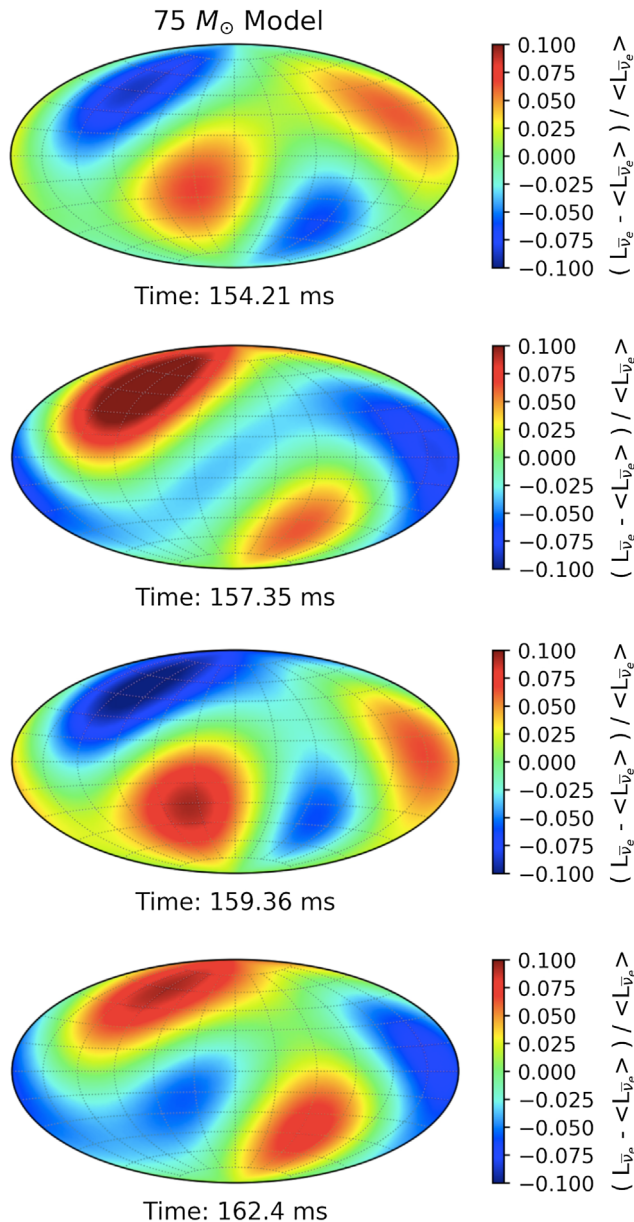
FIG. 8. Molleweide maps of the $\bar{\nu}_e$ luminosity relative to its 4π average for the 75 $M_\odot$ model for four consecutive time snapshots in [140, 175] ms where the SASI quadrupolar motions are dominant (see Fig. 5). The quadrupolar structure of the neutrino emission is clearly visible across the four snapshots. This explains the quasiperiodic, directionally independent signal modulations visible in Fig. 4.

consistent with the dominance of the spiral SASI mode in the 40 $M_\odot$ model, where the shock radius during most of the postbounce evolution (until shortly before BH formation) is larger than in the 75 $M_\odot$ model between 140 ms and 175 ms. The development of the SASI spiral mode is evidenced by the dominance of the neutrino emission dipole over the emission quadrupole in [175, 230] ms in the right panels of Fig. 5. This transition between an $l = 2$ (quadrupolar) and an $l = 1$ (spiral) SASI mode is triggered by the rapid shock expansion that is caused by the drop in the mass accretion rate, in agreement with the findings of Refs. [9,96–100], and it is reflected in the neutrino signal, as also discussed in Ref. [88], in which failed and successful explosions were compared.

The bottom panels of Fig. 6 display the evolution of the $\bar{\nu}_e$ luminosity dipole moment. The left panel shows that the $\bar{\nu}_e$ dipole direction oscillates only within a 90° slice in one hemisphere during the SASI I phase of the 75 $M_\odot$ model in [140, 175] ms (see also the right panel of Fig. 7). This is compatible with the dominant quadrupolar SASI during this time interval of small shock radius. The bottom right panel of Fig. 6 depicts the evolution of the $\bar{\nu}_e$ luminosity dipole during the spiral SASI episode (SASI II), where the dipole vector describes a circular path around the whole sphere (see alsothe right panel of Fig. 7). Clearly, the spiral SASI plane is stationary for the 75 $M_\odot$ model. The moment preceding BH formation is marked by a steep decay of the luminosity dipole at ≃230 ms. This, in turn, is also visible as a damping of the spiral SASI modulations in Fig. 4.

V. LESA IN BLACK HOLE–FORMING MODELS

In Ref. [14], a large hemispheric dipolar asymmetry in the electron-lepton number (ELN) neutrino flux was found in the 3D simulations of 11.2 $M_\odot$, 20 $M_\odot$, and 27 $M_\odot$ SN models. These findings have been confirmed in Refs. [42,59] and, more recently, in Refs. [49,51,88,101]. LESA is thought to originate from hemispherically asymmetric convection in the PNS, which induces regions of excess of ν_e relative to $\bar{\nu}_e$ in the PNS convective layer [14,101]. This, in turn, leads to the development of large-scale asymmetries in the ELN flux and other medium-related properties, e.g., a hemispheric asymmetry of the electron fraction in the PNS [14]. On the other hand, also SASI motions of the postshock layer can produce dipole and quadrupole modes in the neutrino emission as discussed in Sec. IV. In the following, we attempt to discriminate the LESA and SASI asymmetries in the neutrino signal.

To quantitatively characterize the ELN emission asymmetries (caused by LESA or SASI), we estimate the relative excess of ν_e over $\bar{\nu}_e$ emission for each angular direction (θ, ϕ) [14]

$$\Sigma = \frac{1}{T} \int_{t_1}^{t_2} \frac{N_{\nu_e} - N_{\bar{\nu}_e}}{\langle N_{\nu_e} + N_{\bar{\nu}_e} \rangle}, \tag{1}$$

with $T = t_2 - t_1$ being the time interval where the relative excess is estimated, $N_{\nu_e, \bar{\nu}_e}$ being the electron (anti)neutrino number flux, and $\langle N_{\nu_e, \bar{\nu}_e} \rangle$ being the corresponding 4π average of the neutrino number flux.

We use Eq. (1) to estimate the strength of the long-time stable ELN emission asymmetries in our BH-forming models, and for that average over sufficiently long time intervals to smooth out the short-timescale SASI variations. The results are shown in Fig. 9. To track any effects due to the presence of stable (in time and space) ELN emission asymmetries, which are likely to be caused by LESA and not SASI, we choose to integrate over three time intervals for each model (i.e., [100, 170], [170, 240], and [450, 500] ms for the 40 $M_\odot$ model, and [130, 150], [150, 180], and [180, 220] ms for the 75 $M_\odot$ model). Both models show a significantly smaller Σ than was previously found in standard core-collapse SN models (see, e.g., Fig. 6 of Ref. [14] and Refs. [42,48,49,51,88] for comparison). The strength of Σ is greatest in the earliest time interval. The weak nature of the emission asymmetries relative to the monopole or direction-averaged electron neutrino and antineutrino emission in these BH-forming models is caused by the very high-mass accretion rate of the PNS before collapse to a BH. The neutrino emission is strongly dominated by the SASI-modulated accretion luminosity.

References [14,42] found that the development of LESA is characterized by an anticorrelation of the relative luminosities of ν_e and $\bar{\nu}_e$ (cf. Fig. 5 of Ref. [14] and Figs. 4, 7, 8, 10, and 11 of Ref. [42]), while SASI induces

fully correlated variations of the ν_e and $\bar{\nu}_e$ luminosities and also a possibly associated ELN dipole. Figure 10 shows the evolution of the luminosity of each neutrino flavor (L_{ν_β}) relative to the time-dependent average luminosity over all directions ($\langle L_{\nu_\beta} \rangle$). The selected observer directions correspond to the coordinates of the $\diamond$ directions shown in Fig. 9 for the 40 $M_\odot$ and 75 $M_\odot$ models. The $\diamond$ direction is the direction along which Σ is maximal for each model in each selected time interval, and thus we expect to see the maximum anticorrelations in the neutrino vs antineutrino emission properties along this direction. Figure 10 shows small anticorrelated displacements of the luminosity variations of ν_e and $\bar{\nu}_e$ outside the SASI intervals, slightly visible for the 40 $M_\odot$ model until ∼200 ms and tiny in the 75 $M_\odot$ model. During the SASI-modulated episodes, a low-level displacement of the ν_e luminosity relative to the $\bar{\nu}_e$ one can be seen (see the panels of Fig. 10 that show the $\diamond$ directions of Fig. 9 during the second and third time intervals). The displacements of ν_e and $\bar{\nu}_e$ peaks in opposite directions are much smaller than those found in Refs. [14,42]. This points to a negligible impact of LESA on the neutrino emission properties in both BH-forming models, much smaller than seen in the previous models. Notably, both BH-forming models are affected by the very strong spiral SASI activity that instead drives the ν_e and $\bar{\nu}_e$ luminosities in phase with each other and rules over the effects of the weak LESA. This subdominance of LESA compared to SASI in the relative luminosity is clearly visible in the inset of Fig. 10.
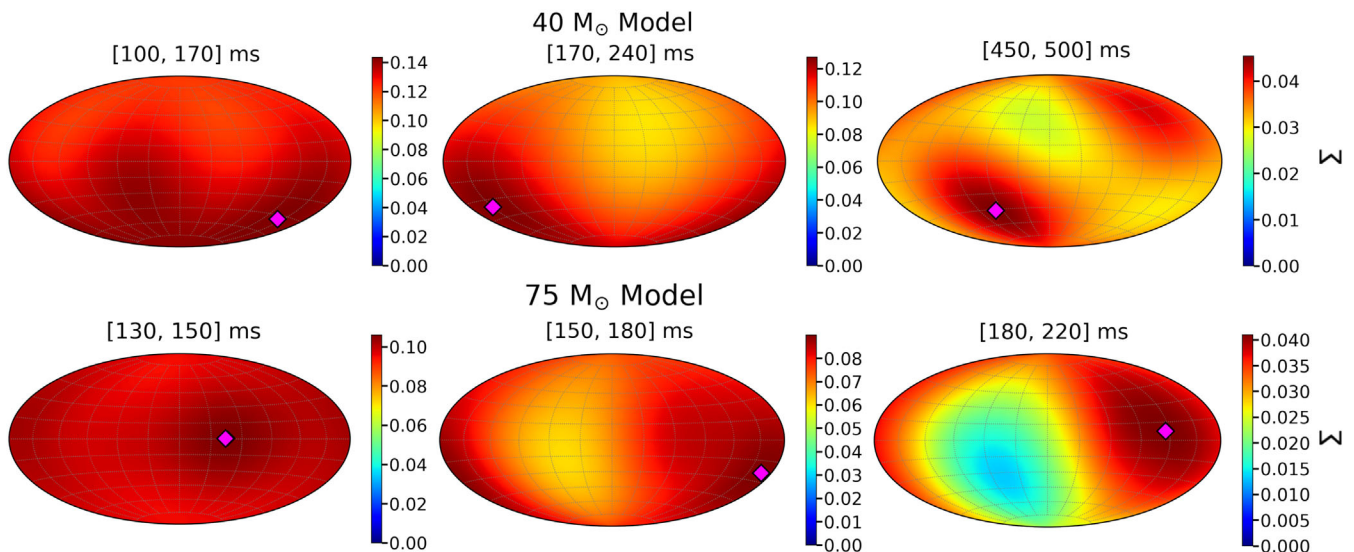

FIG. 9.   Molleweide maps of the Σ parameter [Eq. (1)] for the 40 $M_\odot$ (top) and 75 $M_\odot$ (bottom) models for three selected time intervals (from left to right, respectively). The time intervals have been chosen to track the evolution of the ELN dipole moment. The differences in magnitude of Σ between hot and cold regions correspond to LESA activity because the time averages smooth out short-time variations due to SASI emission modulations. Σ is smaller in these BH-forming models in comparison to other core-collapse SN models previously analyzed (cf. e.g., Fig. 6 of Ref. [14]). The Σ parameter is largest in the earliest time interval (leftmost panels) which has been integrated for both models from $\mathcal{O}(100)$ ms postbounce until approximately the start of the first SASI episode for each model. The $\diamond$ marker indicates the location where Σ is maximal in each selected time interval for each model.
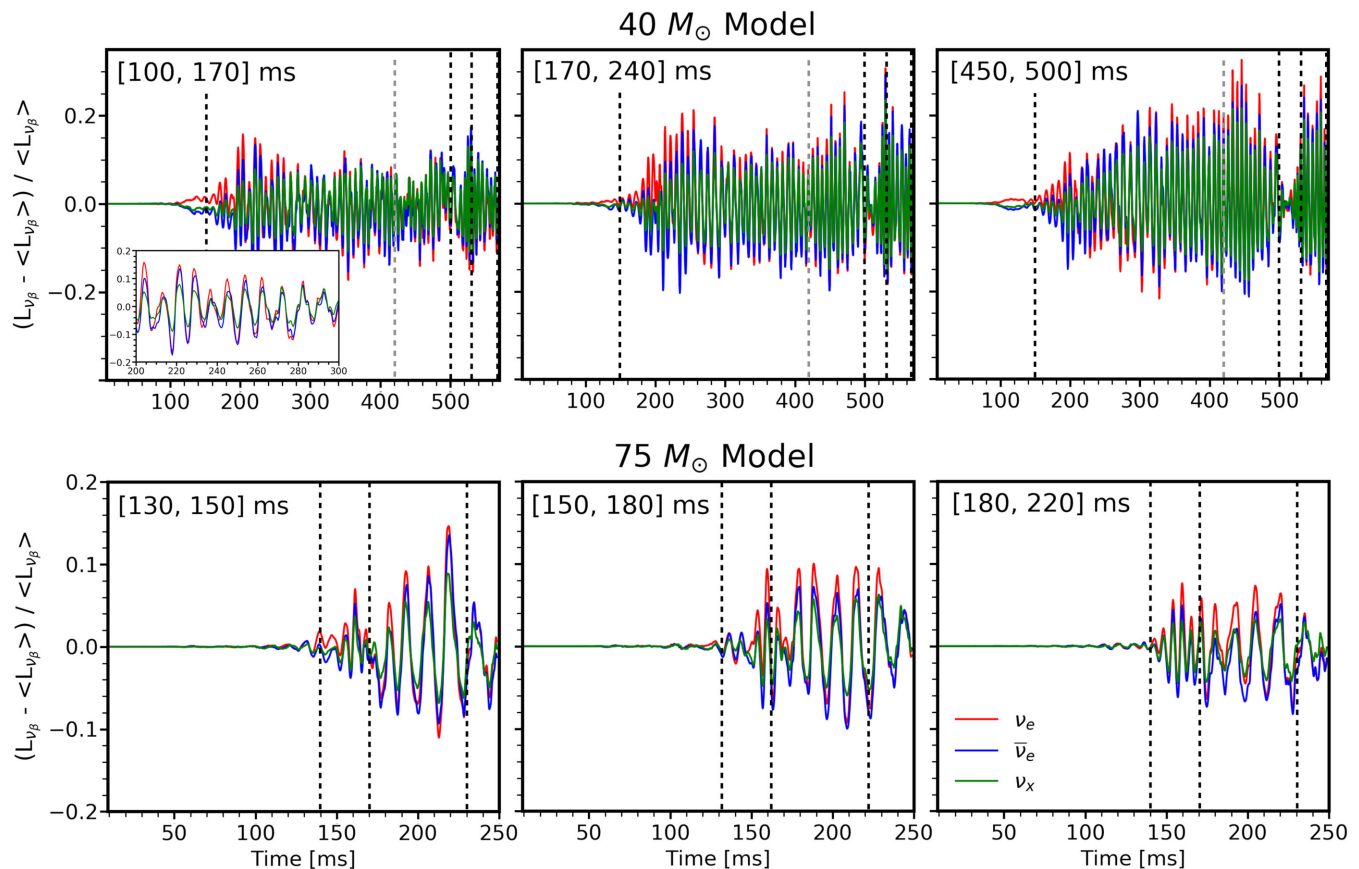
FIG. 10.   Luminosity evolution of each neutrino flavor (L_{ν_β}) for the 40 $M_\odot$ (top) and 75 $M_\odot$ (bottom) models along the ⋄ directions (selected for each time interval as indicated in Fig. 9) relative to the time-dependent average luminosity over all directions ($\langle L_{\nu_\beta} \rangle$). The dashed lines mark the SASI intervals. Because of LESA, the luminosity variations of ν_e and $\bar{\nu}_e$ show a small anticorrelated displacement. The inset in the top left panel highlights only a minimal anticorrelated displacement of the ν_e signal to the positive side and of the $\bar{\nu}_e$ signal to the negative side, because at later times, the ⋄ direction moves to different locations. The shift of the ν_e relative to the $\bar{\nu}_e$ luminosity is much smaller than in Fig. 5 of Ref. [14] and Figs. 4, 7, 8, 10, and 11 of Ref. [42]. These findings suggest that the LESA activity affects the neutrino emission on a very low level.

Both the LESA phenomenon and SASI-modulated accretion are responsible for inducing a dipole (quadrupole) in the ELN emission [42]. To quantify the time evolution of the ELN multipoles and decipher any features due to LESA, we adopt a decomposition in spherical harmonics of the ELN emission following Sec. IV B of Ref. [48]. Figure 11 shows the time evolution of the ELN monopole, dipole, and quadrupole ($A_{ELN,0}$, $A_{ELN,1}$, and $A_{ELN,2}$, respectively). For both models, the dipole and quadrupole are comparable in amplitude to those of other core-collapse SN models; see, e.g., Fig. 3 of Ref. [14] and Fig. 10 of Ref. [48] for a direct comparison among SN models from this group as well as Ref. [49,51,88]. For the 40 $M_\odot$ model, a growing dipole (quadrupole) is observable before ∼150 ms (in correspondence with the LESA anticorrelation between the ν_e and $\bar{\nu}_e$ relative luminosities visible in Fig. 10), but the monopole is much larger. As the SASI I and SASI II phases kick in, a short-time variable dipole (quadrupole) is observable. For the 75 $M_\odot$ model, the ELN quadrupole (dipole) appears mostly due to the SASI quadrupole

(dipole); in fact, the ELN quadrupole (dipole) in Fig. 11 grows in the same time interval when the ν_e and $\bar{\nu}_e$ relative luminosities are almost fully correlated in Fig. 10, and the LESA anticorrelation between the ν_e and $\bar{\nu}_e$ relative luminosities is minimally visible in Fig. 10. Our findings lead us to conclude that, in the present BH-forming models, the accretion luminosity and its SASI modulations largely dominate the neutrino emission; as a consequence, the SASI dipole and quadrupole are mainly visible, whereas the LESA multipoles are hardly visible or not at all. As we will see in the following, also other signatures of LESA are only weakly developed in these BH-forming models.

Reference [14] showed that, once the ELN dipole due to LESA is developed, its direction remains essentially stable (see, e.g., their Fig. 1). Figure 12 shows the evolution of the ELN dipole direction for both BH-forming models. To distinguish between LESA and SASI, the $\bar{\nu}_e$ luminosity dipole direction is also plotted in gray to guide the eye (see also our Fig. 6 and/or Fig. 14 of Ref. [42] for comparison). It is evident that the $\bar{\nu}_e$ dipole direction and the ELN dipole
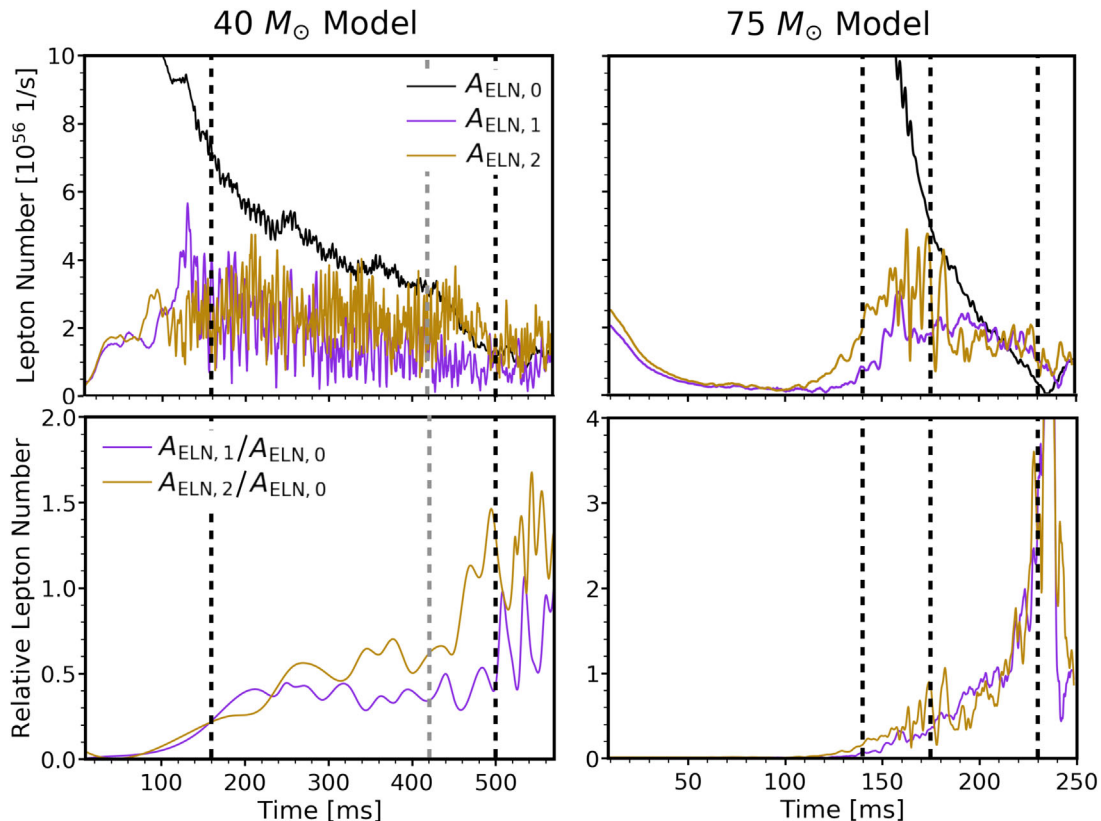
FIG. 11. Time evolution of the amplitudes of the ELN multipole moments for the 40 $M_\odot$ (left) and 75 $M_\odot$ (right) BH-forming models. The dashed lines mark the SASI intervals. *Top:* Evolution of the ELN monopole $l = 0$ (in black), the dipole $l = 1$ (purple), and the quadrupole $l = 2$ (gold). *Bottom:* Evolution of the ELN dipole (purple) and quadrupole (gold) relative to the monopole (in the bottom left panel, the curve has been smoothed to highlight the temporal evolution despite the high-frequency fluctuations). The ELN dipole and quadrupole are comparable in absolute values to the ones previously found in core-collapse SN models (see, e.g., Fig. 3 of Ref. [14] and Fig. 10 of Ref. [48] for a direct comparison). However, the monopole is larger, and the dipole and quadrupole of the ELN emission are mainly driven by the strong (short-time modulated) spiral SASI activity responsible for an ELN accretion dipole (quadrupole) in these BH-forming models (see Fig. 10 for comparison).

direction are not correlated; both develop basically independently. This is a clear signature that both do not originate only from a single (hydrodynamical) phenomenon. While the $\bar{\nu}_e$ emission dipole results mainly from SASI-induced accretion modulations, the ELN dipole is a superposition of effects from SASI and LESA. The nonstationary drifting of the ELN dipole suggests that the SASI-ELN dipole dominates over the LESA-ELN dipole and the migration of the ELN dipole is mainly a consequence of the strong and long-lasting SASI activity. This is especially evident in the 40 $M_\odot$ model, where the spiral SASI-induced accretion and neutrino-emission modulations are particularly fast (because of the small shock radius) and their relative amplitudes are considerably larger than in the 75 $M_\odot$ case.

Finally, the LESA instability is responsible for generating a dipole in the electron fraction (Y_e) around the PNS convection layer [14,49,51,59,88,101]. Figure 13 shows the evolution of the electron fraction distribution in the PNS for the 40 $M_\odot$ (top) and 75 $M_\odot$ (bottom) models. From left

to right, for each of the selected observer directions, the cut plane is chosen in such a way to contain the ELN dipole vector and the z axis of the data grid (see Fig. 11 and Sec. V of Ref. [48] for more details). The black arrows point in the direction of the positive ELN dipole moment. Only a very mildly asymmetric deleptonized shell develops in both models as a direct signature of the weak LESA activity. Therefore, no clear dipole asymmetry of the Y_e distribution is visible in directional correlation with the ELN dipole vector. Again, this suggests that the nonstationary dipole of the ELN emission is mostly associated with the SASI accretion emission.

Clear indicators of LESA asymmetries in the PNS are obviously much weaker than in our previously analyzed models. LESA has been argued to be a consequence of asymmetric PNS convection [14,59,101]. Hence, we interpret our findings as a consequence of the fact that the PNS convection layer in the BH-forming models is deeper inside the PNS core. This means that the neutrino diffusion timescale from the convective layer through the overlying,
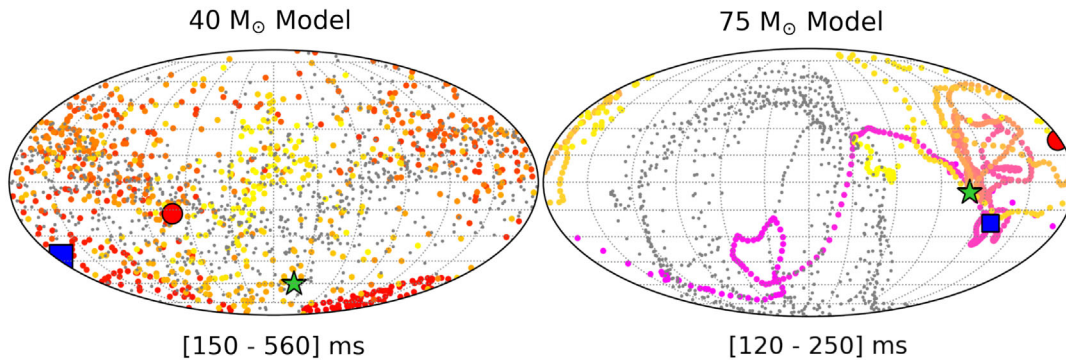
FIG. 12.   Time evolution of the direction of the ELN dipole moment for the 40 $M_\odot$ (left) and 75 $M_\odot$ (right) models during the time intervals when the ELN dipole is dominant or equally strong as the quadrupole. The colorful dots mark the path of the positive ELN dipole direction, and the color hues become lighter as time increases. The gray dots mark the path of the positive $\bar{\nu}_e$ luminosity dipole moment following the spiral SASI evolution (see Fig. 6). In each map, the markers indicate the directions of the positive ELN dipole at the three time snapshots depicted in Fig. 13. The ELN dipole does not reach stationary conditions for the 40 $M_\odot$ model, but instead rapidly wanders across the whole emission surface. The dipole migrates only within one-half of the emitting surface in the 75 $M_\odot$ model, given the more slowly varying and lower-amplitude spiral SASI accretion and neutrino-emission modulations in this model (because of its large shock radius). In both cases, the dipole never reaches a stationary location. The fact that the $\bar{\nu}_e$ and ELN emission dipoles are not closely correlated but evolve independently signifies that they do not originate from a single effect, but SASI and LESA both play a role.
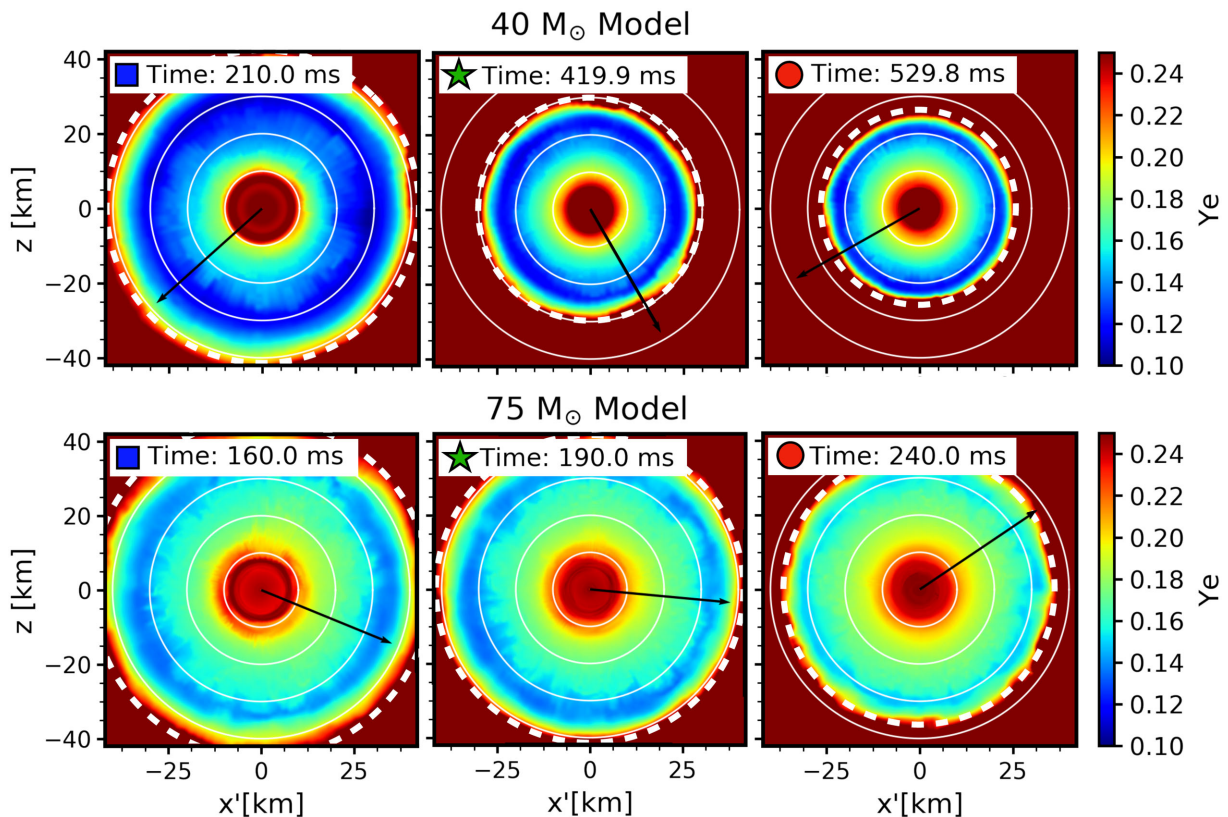

FIG. 13.   Distribution of the electron fraction, Y_e, in the PNS for the 40 $M_\odot$ (top) and 75 $M_\odot$ (bottom) models at the three indicated postbounce times. For each selected angular direction (from left to right, see directions marked on Fig. 12), the cut plane is chosen in such a way to contain the ELN dipole vector and the z axis of the polar grid for the data (see Fig. 11 and Sec. V of Ref. [48] for more details). The plots are oriented in such a way that the north and the south poles of the data grid are at the top and bottom, respectively. The white circles indicate radii at every 10 km to guide the eye, and the white dashed circles highlight the location of the PNS radius. The black arrows point in the direction of the positive ELN dipole moment. A marginally asymmetric shell with slightly stronger deleptonization in the direction of minimal lepton number flux is present within the PNS convection zone in some snapshots, but the effect is by far not as pronounced as in our previous models.

massive, dense accretion mantle to the neutrinosphere in the present models is longer than in lower-mass progenitors with lower accretion rates. This fact may delay or hamper the development of a pronounced LESA emission asymmetry and a correspondingly asymmetric electron distribution in the PNS convection layer. On the other hand, in Refs. [88,102], it was found that a higher PNS mass is associated with stronger convection, as a consequence of the deeper gravitational potential well generated by the heavier PNS mass.

The authors of Ref. [88] reported clear signatures of LESA in the neutrino emission of all of their models, with a strong ELN dipole appearing at or shortly after ∼200 ms in all cases. For all of their models, they witnessed a clear correlation between the orientation of the LESA dipole axis and the dipole axis of the Y_e distribution in the convective PNS (in agreement with Refs. [14,42,47,48,51,59,101]), but no strong evidence that LESA correlates with either the behavior of the shock surface or the accretion rate. We do not consider the findings of Ref. [88] to be in conflict with our interpretation. In all of the models of Refs. [88,102], the mass accretion rate of the PNS has dropped below (in most cases even considerably below) 1 $M_\odot$ s^{-1} at the time when the ELN dipole amplitude begins to compete with the monopole of the lepton-number emission, either because the star is exploding or because the nonexploding models are $13 - 15\ M_\odot$ progenitors with generically lower accretion rates. This is in line with what we discussed in Refs. [14,42,47,48] for the lower-mass models presented there. In contrast, the high-mass models discussed here possess mass accretion rates of at least 1 $M_\odot$ s^{-1} until the end of the simulated evolution, and during most of the postbounce time even significantly higher values (see Fig. 1, top panel). Therefore, the accretion luminosity is considerably larger and the accretion contribution to the anisotropic ELN emission correspondingly bigger in our BH-forming models.

VI. DETECTABLE FEATURES IN THE NEUTRINO SIGNAL

Neutrinos are among the only potentially detectable probes of a massive star collapsing into a BH. In this section, we focus our attention on the detectable characteristics of the emitted neutrino signal and identify which of the physical features discussed above can be directly inferred from measurable quantities. To this purpose, we estimate the event rate detectable in IceCube, Super-Kamiokande, and in the Deep Underground Neutrino Experiment (DUNE) for the two BH-forming models.

A. Neutrino flavor conversions

The neutrino signal observed in a detector on Earth is crucially affected by the flavor conversion history along the way. Flavor conversions are neglected in the neutrino

transport equations in SN simulations, under the assumption that the propagation eigenstates coincide with the weak-interaction eigenstates because of the strong matter effect [103]. However, as neutrinos stream away from the SN core and the matter background decreases, flavor conversions become important; see, e.g., Refs. [34,104] for recent reviews on the topic.

Adiabatic neutrino flavor conversions occur because of the SN matter background felt by neutrinos, the so-called Mikheev-Smirnov-Wolfenstein (MSW) effect. According to this picture, a detector mainly sensitive to $\bar{\nu}_e$ will see a neutrino energy distribution roughly given by 70% of the unoscillated $\bar{\nu}_e$ energy distribution and 30% of the unoscillated $\bar{\nu}_x$ distribution for normal mass ordering. On the other hand, for inverted ordering, the detected $\bar{\nu}_e$ energy distribution will coincide with the unoscillated $\bar{\nu}_x$ distribution at the source. Similarly, a detector sensitive to ν_e will basically detect the unoscillated ν_x for normal ordering, and a linear combination of the unoscillated energy distributions of ν_e and ν_x for inverted ordering.

Such a simple picture can be strongly modified in two ways. First, if the radial profile of the matter background has significant stochastic fluctuations, this would be responsible for affecting the adiabaticity of the flavor conversions, as it happens in the presence of turbulence [105,106]. The second way is if the neutrino-neutrino refraction is not negligible, which is usually the case at radii smaller then the ones where MSW effects take place. What exactly happens when neutrino-neutrino interactions dominate the flavor evolution history remains poorly understood because of the nonlinear nature of the phenomenon. In particular, it has been recently postulated that neutrino-neutrino interactions occurring in the proximity of the SN core may occur at a "fast" rate determined by the neutrino density and possibly lead to flavor equilibration; see, e.g., Refs. [107–109].

Given the current uncertainties on our understanding of flavor conversion of SN neutrinos, we refrain from considering any specific flavor conversion scenario, and instead rely on the unoscillated neutrino signal. Independently of the exact mixing outcome, the real signal detected on Earth will be an intermediate case between the $\bar{\nu}_e(\nu_e)$ unoscillated signal (mimicking what one would detect in the absence of flavor conversions) and the $\bar{\nu}_x(\nu_x)$ unoscillated signal (mimicking what one would detect under the assumption of full flavor conversions).

As for the neutrino energy distribution, it was demonstrated in Refs. [42,110] that the unoscillated neutrino energy distribution of all flavors can be fitted with extremely high accuracy with a Gamma distribution. Therefore, in the following, we will rely on the neutrino luminosity, mean energy, and second energy moment to reconstruct the neutrino fluence expected on Earth and the related event rate.

B. Expected neutrino event rate

The neutrino detector currently providing the largest event statistics for a Galactic SN is the IceCube Neutrino Observatory [61]. This Cherenkov detector works mainly through the inverse-beta-decay ($\bar{\nu}_e + p \rightarrow n + e^+$) channel and is mainly sensitive to the $\bar{\nu}_e$ flux. We estimate the IceCube event rate for each BH-forming model using the method outlined in Sec. V of Ref. [42] and folding
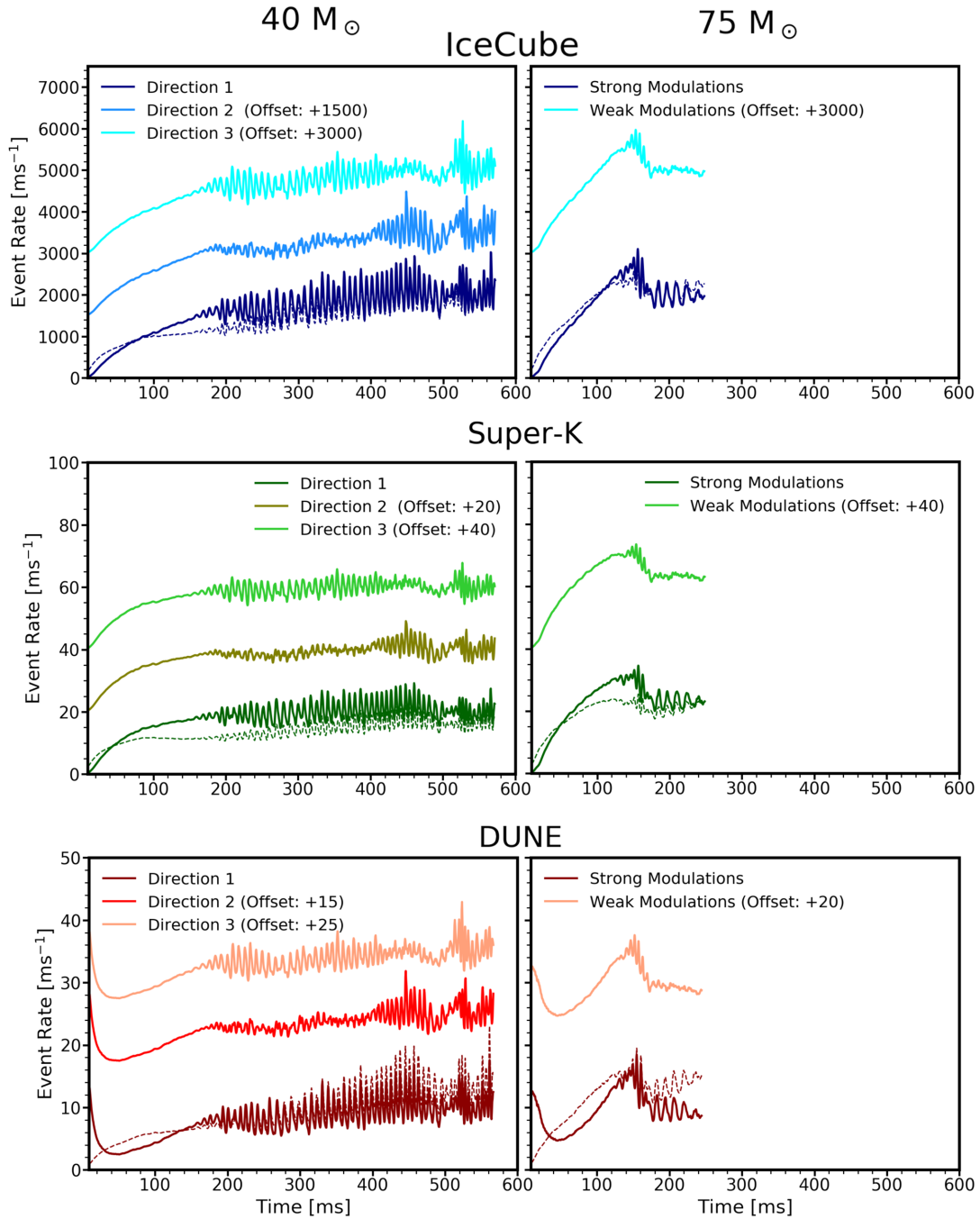

FIG. 14.   Expected detection rate for the 40 $M_\odot$ (left) and 75 $M_\odot$ (right) models as a function of postbounce time for a stellar collapse located at 10 kpc. The event rate is plotted for IceCube, Super-Kamiokande, and DUNE from top to bottom, respectively. In the top and middle panels, the event rate along direction 1 has been plotted for $\bar{\nu}_e$ (continuous line, absence of flavor conversion) and for ν_x (dashed line, full flavor conversion). The three different colors indicate the observer directions chosen as detailed in Sec. III B. For simplicity, the $\bar{\nu}_e$ signal without flavor conversions has been adopted for the other observer directions. Similarly, the bottom panels show the corresponding event rates in DUNE, for the main $\nu_e - ^{40}$Ar detection channel. In all cases, the event rate mirrors the SASI signal modulations for both models.

the neutrino energy distribution with the inverse-beta-decay cross section [111]. The event rate is computed assuming an overall background rate $R_{bkgd} = 1.48 \times 10^3$ ms^{-1} [61].

The signal modulations developing in the BH-forming stellar collapse will also be detectable by the water Cherenkov detector Super-Kamiokande [42,62]. Super-Kamiokande has a fiducial volume of 22.5 kton and is also mainly sensitive to $\bar{\nu}_e$, albeit with fewer statistics than IceCube. Notably, Super-Kamiokande has the advantage of being virtually background free for SN neutrino detection ($R_{bkgd} = 0$). For the estimation of the expected event rate, we employ the same inverse-beta-decay cross section as for IceCube and assume a 100% detector efficiency for Galactic SNe [112].

The top panels of Fig. 14 show the predicted IceCube event rate for the 40 $M_\odot$ (left) and 75 $M_\odot$ (right) models for an observer located along the directions selected in Sec. III B and for a SN located at a distance of 10 kpc. Each predicted signal exhibits clear large-amplitude modulations due to spiral SASI for observers located in the proximity of the SASI planes, similar to what was found for the 15 $M_\odot$, 20 $M_\odot$, and 27 $M_\odot$ models in Refs. [42,43,47]. Remarkably, however, due to the strong spiral SASI activity, the modulations in the neutrino signal will also be visible for the 40 $M_\odot$ model for observers located away from the main SASI planes. Additionally, the quadrupolar SASI phase of the 75 $M_\odot$ model in the interval [140, 175] ms is also clearly detectable along any given observer direction. These features present in the neutrino signal will also be detectable by Super-Kamiokande, as shown in the middle panels of Fig. 14, although with a reduced event rate. As visible from Fig. 14, BH-forming stellar collapses are expected to have a slightly increased event rate than ordinary core-collapse SNe (see, e.g., Refs. [42,43,45,90,113] for comparison).

Figure 15 shows the detection significance of the time-integrated neutrino burst preceding the BH formation, as a function of distance,

$$\sigma = \frac{N_{ev}}{\sqrt{N_{bkgd}} + \sqrt{N_{ev}}}, \qquad (2)$$

where N_{ev} is the total number of SN neutrino events integrated over the signal duration at a chosen distance from the BH-forming stellar collapse event and N_{bkgd} is the total number of background events in the same time window. The left panel of Fig. 15 shows that a BH-forming event will be detectable at more than 3σ by IceCube up to $\mathcal{O}(100)$ kpc. For comparison, the middle panel shows the detection significance of Super-Kamiokande. Here, the burst prior to BH formation will be detectable in neutrinos up to $\mathcal{O}(250)$ kpc due to the absence of background in Super-Kamiokande over the relatively small time window of a SN burst.

Given the strong spiral SASI activity of the models investigated in this paper and the high event rate for BH-forming models expected from IceCube and Super-Kamiokande, we foresee that the characteristic neutrino signatures will also be visible in the upcoming DUNE neutrino detector [63]. DUNE is a 40 kton liquid-argon time projection chamber planned to be in complete operation within 2026. The main detection channel for low-energy neutrinos will be the charged current absorption of electron neutrinos on ^{40}Ar ($\nu_e + {}^{40}$Ar $\rightarrow e^- + {}^{40}$K*) with an energy threshold of 5 MeV and a planned detection efficiency of 86% [63].

Similarly to the IceCube and Super-Kamiokande event rates, the DUNE event rate can be estimated by folding the emitted neutrino flux with the $\nu_e - {}^{40}$Ar cross section provided in Ref. [63] and by taking into account the
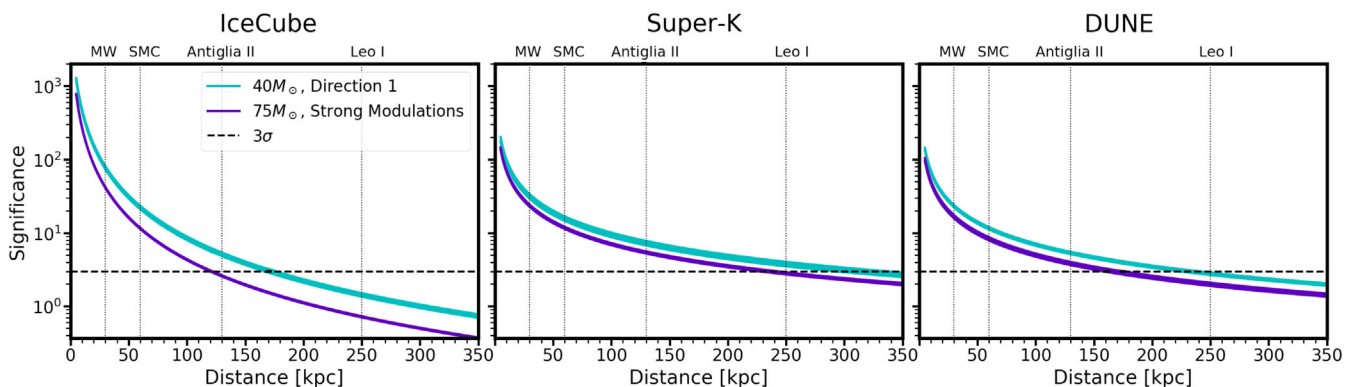

FIG. 15. Detection significance of the neutrino burst from BH formation for the 40 $M_\odot$ (cyan) and 75 $M_\odot$ (purple) models as a function of the BH-forming collapse event distance for the IceCube Telescope, Super-Kamiokande, and DUNE, from left to right. For both models, the direction yielding the highest number of events has been chosen (i.e., direction 1 for the 40 $M_\odot$ model and the strong modulations direction for the 75 $M_\odot$ model). The bandwidth in each detection significance curve reflects the two extreme flavor oscillation scenarios. The black dashed horizontal line marks the 3σ detection significance. The vertical dotted lines mark the edge of the Milky Way as well as the Small Magellanic Cloud, Antiglia II, and Leo I. The detection of the neutrino burst with DUNE and Super-Kamiokande will be more likely than for IceCube at large distances since these detectors are virtually background free.

detection efficiency. The bottom panels of Fig. 14 show the predicted neutrino event rate in DUNE as a function of time for the 40 $M_\odot$ (left) and 75 $M_\odot$ (right) models along the observer directions selected in Sec. III B and at a distance of 10 kpc. The main background for the detection of neutrinos from stellar collapse events is thought to be about 122 solar neutrinos per day [63]. As it can be seen from the bottom panels of Fig. 14, this background rate is negligible compared to the event statistics of the neutrino burst from BH-forming stellar collapse events. Thus, we set $R_{bkgd} = 0$, similar to what is considered for Super-Kamiokande. The total expected number of events for the 75 $M_\odot$ model increases by $\simeq 30\%$ on average, if the charged current absorption of $\bar{\nu}_e$ on ^{40}Ar and the neutral current scattering of all flavors on ^{40}Ar are included. The gap between the event rates of ν_e and the heavy lepton flavors clearly visible in the bottom right panel of Fig. 14 becomes increasingly large as the postbounce time increases, because in this particular model, the emitted flux of ν_e's drops continuously after the infall of the Si/O interface while the flux of $\bar{\nu}_e$ and ν_x increases.

As shown in the right panel of Fig. 15, the detection of neutrinos from BH-forming collapse events in DUNE will occur with a significance larger than 3σ for bursts located up to 170 kpc for the 75 $M_\odot$ model and 240 kpc for the 40 $M_\odot$ model. In fact, although Super-Kamiokande and DUNE will have fewer statistics than IceCube (see Fig. 14), the detection of neutrinos from stellar core-collapse events with these detectors will be more promising than for IceCube at large distances since these detectors are virtually background free. This feature is very encouraging for what concerns the detection of BH-forming collapse events in neutrinos.

C. Fourier analysis of the event rate

In this section, we further identify the detectable features of SASI unique to BH formation by studying the frequency content of the neutrino event rate of the two BH-forming models in Fig. 14. For this, we investigate the spectrograms of the neutrino event rate obtained as detailed in Sec. IV of Ref. [47] and the power spectrum of the neutrino event rate, computed following Ref. [46].

Figure 16 shows the spectrograms of the IceCube event rate for the 40 $M_\odot$ model along the three observer directions selected in Sec. III B. Each spectrogram is normalized to the maximum Fourier power along the selected observer direction. Along direction 1, the first spiral SASI episode is identifiable through the stripe in hotter colors appearing in correspondence to the spiral SASI frequency [$\mathcal{O}(100)$ Hz]. Remarkably, given the long-lasting spiral SASI phase, the hot red region of the spectrogram clearly highlights dips and peaks as well as an overall increase of the SASI frequency as a function of time. These trends can be explained by taking into account that the spiral SASI frequency depends on the shock radius and on the NS radius in the following way [9],

$$f_{SASI}^{-1} \simeq \int_{R_{NS}}^{R_s} \frac{dr}{|v|} + \int_{R_{NS}}^{R_s} \frac{dr}{c_s - |v|}, \qquad (3)$$

where c_s is the radius-dependent sound speed and v is the accretion velocity in the postshock layer. As can be seen in Fig. 1, in the 40 $M_\odot$ model, the shock radius contracts reaching a local minimum around 200 ms, and then it slightly expands around 300 ms until it reaches a stationary value; correspondingly, R_{NS} contracts, and the postshock velocity tends to follow a trend opposite to the shock radius
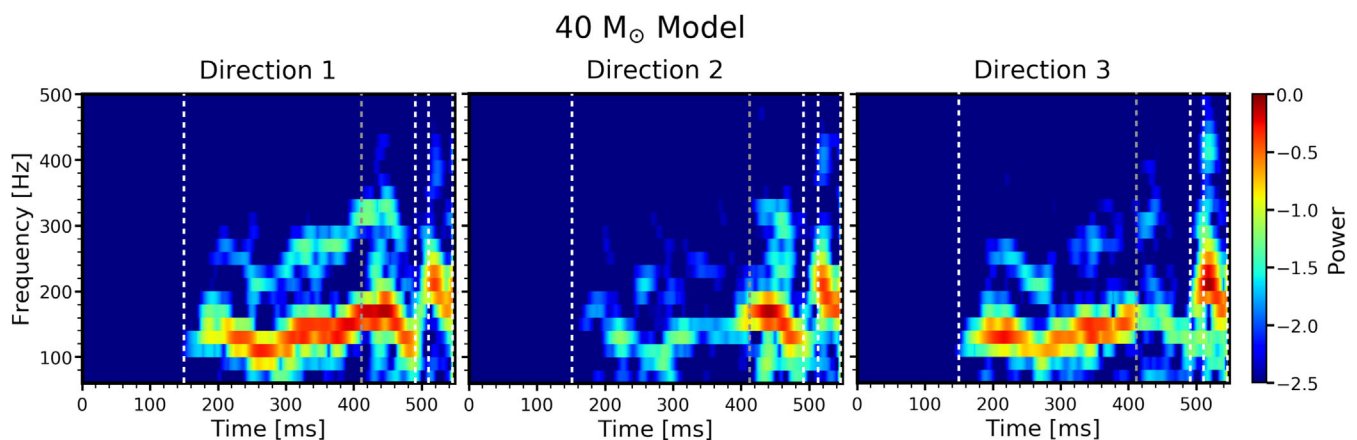

40 $M_\odot$ Model

FIG. 16. Spectrograms of the $\bar{\nu}_e$ IceCube event rates in the absence of flavor conversions for the 40 $M_\odot$ model along the three directions chosen in Sec. III B. The spectrogram power has been normalized to the maximum Fourier power along each selected observer direction and plotted on a log color scale. Dashed vertical lines indicate the same SASI intervals as in Fig. 3, but extend forward in time by 10 ms to compensate for the effects of the sliding window over which the short-time Fourier transform is computed. Because of the 50 ms sliding window, the plotted spectrograms end 25 ms before the end of the simulation. The spiral SASI activity is characterized by hot red regions in the spectrograms. The evolution of the spiral SASI frequency is clearly visible. Negligible activity is found for frequencies larger than 500 Hz.

(smaller shock radii lead to higher magnitudes of the postshock velocity and vice versa); see Figs. 1 and 3. Therefore, the SASI frequency tends to decrease during phases of shock expansion and to increase during periods of shock retraction. Thus, in Fig. 16, one can clearly see that f_{SASI} tracks the shock contraction and expansion preceding the onset of BH formation, in agreement with what was diagnosed in Refs. [96,114] and still holds in the case of the spiral SASI.

Notably, even the spectrogram of the signal along direction 2 (i.e., along one of the least optimal directions for observing the modulations in the first subinterval of the long spiral SASI episode) shows clear signs of the evolution of the spiral SASI frequency in time. The less prominent, but still traceable, hot region in the first subinterval, [160, 420] ms, lines up perfectly with the brighter hot region in the second subinterval, [420, 500] ms, as it does along directions 1 and 3. Also, along direction 3, the colored regions line up at the boundary between the two subintervals ($t_{p.b.} \simeq 420$ ms), indicating that the hot region in [420, 500] ms marks a continuation of the spiral SASI episode along a slightly different direction.

Figure 17 gives the spectrograms of the IceCube event rate for the 75 $M_\odot$ model along the two observer directions chosen in Sec. III B. As expected, the hot red region corresponding to the spiral SASI frequency in the interval [175, 230] ms nearly disappears between the strong (left) and weak (right) modulation directions. The frequency of the quadrupolar SASI modulations in the IceCube event rate in the interval [140, 175] ms is represented by a hot red region, visible as expected in both spectrograms due to their directional independence. The left-hand panel shows that the spiral SASI dipole frequency is clearly lower than the

frequency of the SASI quadrupolar motion. In fact, as visible from Fig. 1, for the 75 $M_\odot$ model, the relative difference $R_s - R_{NS}$ grows as a function of time as R_s expands and R_{NS} contracts, and this is responsible for a drop of the SASI frequency from the quadrupolar to the dipolar phase [115]. As previously discussed in Sec. IV, at the transition between the quadrupolar and the dipolar phase, the shock radius shows a contraction followed by an expansion (between 130 and 160 ms just before the approach of the Si/O interface) that is also tracked by the drop of the SASI frequency in the same time interval. Similar information should also be contained in the spectrograms of the correspondent gravitational wave signal [45,90,116–118]. However, a dedicated analysis of the imprints of BH formation in the gravitational wave signal will be subject of a future paper.

Figure 18 shows the Fourier power spectra of the IceCube event rate for the 40 $M_\odot$ (left) and the 75 $M_\odot$ models (right), normalized to the power of a shot noise realization of the IceCube background event rate (R_{bkgd}). On the left-hand side, the power spectrum for the 40 $M_\odot$ model has been computed in the interval of the first spiral SASI episode, [160, 500] ms, along each of the three observer directions selected as in Sec. III B. Two different frequency peaks can be clearly identified, one at ~110 Hz and the other one at ~130 Hz, corresponding to the spiral SASI frequency in [160, 420] ms and [420, 500] ms subintervals, respectively. Thus, there is an increase in frequency of about 20 Hz as the shock radius retracts. However, this feature will only be detectable along directions where all SASI peaks rise above the power of the shot noise in IceCube. The right panel of Fig. 18 shows the Fourier power spectrum of the 75 $M_\odot$ model. Along the
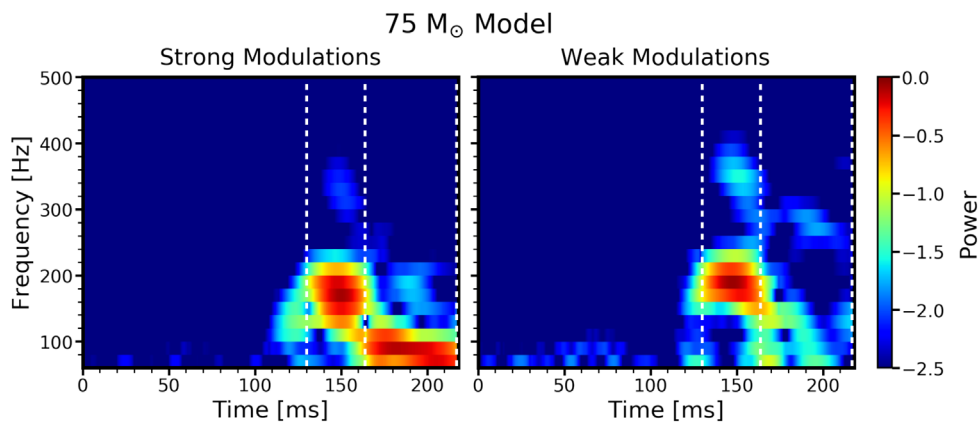

FIG. 17. Spectrograms of the $\bar{\nu}_e$ IceCube event rates similar to Fig. 16, but for the 75 $M_\odot$ model. The left panel shows the strong modulations direction, which lies along the spiral SASI plane, showing activity corresponding to the dipole spiral SASI frequency in the interval [175, 230] ms. This red spiral SASI region nearly disappears along the weak modulations direction as expected. The region corresponding to the quadrupolar SASI modulations in the interval [140, 175] ms is directionally independent and present in both spectrograms. The quadrupolar SASI frequency is higher than the dipolar spiral SASI frequency. Dashed vertical lines indicate the same SASI intervals as in Fig. 4, but extend forward in time by 10 ms to compensate for the effects of the sliding window over which the short-time Fourier transform is computed. Because of the 50 ms sliding window, the plotted spectrograms end 25 ms before the end of the simulation.
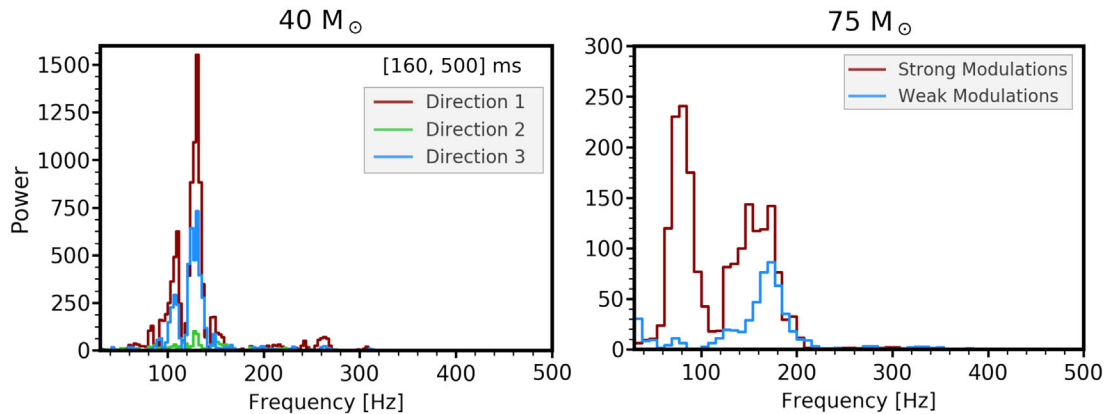
FIG. 18.   Fourier power spectrum of the $\bar{\nu}_e$ IceCube event rate for the 40 $M_\odot$ (left) and the 75 $M_\odot$ models (right) at 10 kpc. Each power spectrum has been normalized to the average power of the IceCube shot noise. In the left panel, the Fourier spectrum for the 40 $M_\odot$ model is plotted along direction 1 (dark red), direction 2 (lime green), and direction 3 (pale blue) selected as in Sec. III B, over the time interval of the first spiral SASI episode. The two separate peaks indicate the dominant spiral SASI frequency in the modulations of the first and second phases of the spiral SASI episode, respectively. A higher "overtone" is visible as low peak around 260 Hz (see also Fig. 16). The Fourier power spectrum of the full $\bar{\nu}_e$ IceCube event rate for the 75 $M_\odot$ model is plotted along the directions of strong (dark red) and weak (pale blue) modulations determined in Sec. III B. The two peaks correspond to the SASI quadrupolar and dipolar activity. The dipolar spiral SASI peak is sharp and prominent, whereas the peak corresponding to the quadrupolar SASI is broader.

strong modulation direction, two peaks can be clearly identified: one corresponding to the dipolar spiral SASI frequency at ~80 Hz and one corresponding to the frequency of the quadrupolar SASI at ~160 Hz, higher than the former [98], as expected due to the contraction of the shock radius. As expected, the peak of the dipole spiral SASI frequency disappears along the weak modulations direction.

Figure 19 presents the detection significance of the spiral SASI peak normalized to the power of the detector noise in the Fourier spectrum of the IceCube, Super-Kamiokande, and DUNE event rates for the 40 $M_\odot$ and the 75 $M_\odot$ models as a function of the SN distance. As discussed in the

previous section, the IceCube noise model includes the shot noise of the detector and statistical fluctuations of the incoming neutrino signal. In Super-Kamiokande and DUNE, which are considered background free over the short time interval of the stellar collapse, the noise model includes only statistical Poissonian fluctuations of the detected neutrino signal. For each model, we choose the direction yielding the highest number of total events, i.e, direction 1 for the 40 $M_\odot$ model, and the strong modulations direction for the 75 $M_\odot$ model. The band is found by considering the two scenarios of absence of flavor conversions or full flavor conversion, as shown in Fig 14. In IceCube, the spiral SASI peak will be distinguishable over
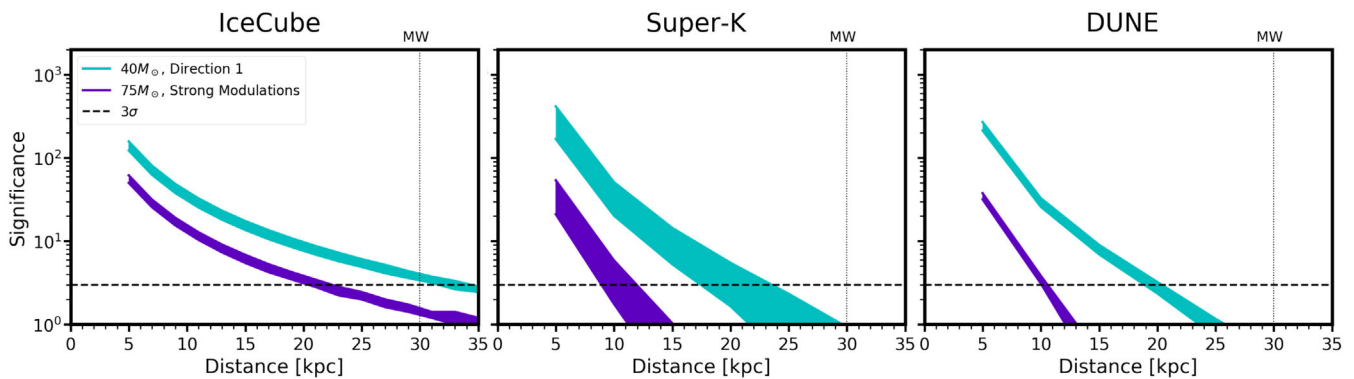

FIG. 19.   Detection significance of the spiral SASI peak in the Fourier spectrum of the IceCube (left), Super-Kamiokande (middle), and DUNE (right) event rates for the 40 $M_\odot$ (cyan) and the 75 $M_\odot$ (purple) models compared to that of the detector noise. Each Fourier decomposition is done for the event rate along the most optimal directions: direction 1 for the 40 $M_\odot$ model and the strong modulations direction for the 75 $M_\odot$ model. The bandwidth in each detection significance curve reflects the two extreme scenarios absent or complete flavor conversion. The black dashed horizontal line marks the 3σ detection significance. The vertical dotted lines mark the edge of the Milky Way. The SASI frequency will be detectable above the detector noise within our own Galaxy.

the detector noise for distances up to 35 kpc for the 40 $M_\odot$ model and ~22 kpc for the 75 $M_\odot$ model, while it will be detectable in DUNE and Super-Kamiokande only up to distances of $\mathcal{O}(10-20)$ kpc.

In conclusion, due to the higher neutrino event statistics, the Fourier power spectrum of the IceCube event rate will be able to determine the SASI frequency at greater distances than DUNE and Super-Kamiokande. However, due to the absence of background in DUNE and Super-Kamiokande, these detectors will be able to detect the neutrino burst from a BH-forming stellar collapse event up to impressively large distances.

VII. CONCLUSIONS

Intriguingly, very little is known about the properties of black hole–forming stellar collapse events. Throughout this work, we aim to provide a first attempt to infer detectable characteristics of the neutrino signal unique to BH formation, by exploring the neutrino emission properties of the 3D hydrodynamical simulations of two BH-forming progenitors with different masses (40 $M_\odot$ and 75 $M_\odot$) and metallicities.

The two models have different BH formation timescales (approximately 570 ms for the 40 $M_\odot$ model and 250 ms for the 75 $M_\odot$ model). Interestingly, while the 75 $M_\odot$ model exhibits a shock expansion before the collapse into a BH, similarly to what was found in Refs [32,57,60], the shock radius evolves toward a quasistationary value in the 40 $M_\odot$ model. The extremely high accretion rate causes the neutrino luminosity to be dominated by accretion luminosity, and the ELN emission dipole and quadrupole are dominated by the rapidly fluctuating spiral SASI-induced modulations of amplitude and direction. The variations of the time-averaged (and in this sense stable) ELN emission with direction, relative to the total neutrino number flux, are considerably weaker than in previous "normal" core-collapse models, and the anticorrelation of the ν_e and $\bar{\nu}_e$ emission variations is much smaller or barely visible. The same holds true for asymmetries of the electron distribution around the protoneutron star convection layer. Altogether, the implications of the neutrino-driven self-sustained asymmetry (LESA) are minor in the BH-forming stellar collapses investigated in this work.

Extremely strong and long-lasting spiral and quadrupolar SASI episodes occur in these models. Since the neutrino event rate for BH-forming stellar collapse is expected to be higher than that of ordinary core-collapse supernovae because of the higher luminosity emitted in neutrinos, the spiral SASI frequency will be detectable by the IceCube Neutrino Telescope for BH formation occurring up to distances of 35 kpc (~22 kpc) for the 40 $M_\odot$ (75 $M_\odot$) models. Similarly, the detection prospects are limited to our own Galaxy for Super-Kamiokande and DUNE.

Notably, given the long-lasting spiral SASI, the evolution of the spiral SASI frequency will be clearly visible, e.g., in the spectrogram of the IceCube event rate. Moreover, SASI imprints will be detectable in neutrinos even for observes located away from the spiral SASI plane because of the strong SASI activity.

The two BH-forming progenitor models explored throughout this work illustrate the phenomenal power of using neutrinos to study the physical processes involved in BH formation. The excellent detectability prospects in neutrinos for these yet mysterious astrophysical events have the potential to unveil the inner workings of collapsing massive stars.

[1] C. L. Fryer, Astrophys. J. **522,** 413 (1999).

[2] S. A. Colgate and R. H. White, Astrophys. J. **143,** 626 (1966).

[3] S. A. Colgate, Astrophys. J. **163,** 221 (1971).

[4] S. E. Woosley, A. Heger, and T. A. Weaver, Rev. Mod. Phys. **74,** 1015 (2002).

[5] H. A. Bethe, Rev. Mod. Phys. **62,** 801 (1990).

[6] H. A. Bethe and J. R. Wilson, Astrophys. J. **295,** 14 (1985).

[7] J. M. Blondin, A. Mezzacappa, and C. DeMarino, Astrophys. J. **584,** 971 (2003).

[8] J. M. Blondin and A. Mezzacappa, Nature (London) **445,** 58 (2007).

[9] L. Scheck, H.-T. Janka, T. Foglizzo, and K. Kifonidis, Astron. Astrophys. **477,** 931 (2008).

[10] W. Iwakami, K. Kotake, N. Ohnishi, S. Yamada, and K. Sawada, Astrophys. J. **700,** 232 (2009).

[11] A. Marek and H.-T. Janka, Astrophys. J. **694,** 664 (2009).

[12] T. Foglizzo, F. Masset, J. Guilet, and G. Durand, Phys. Rev. Lett. **108,** 051103 (2012).

[13] R. Fernàndez, Astrophys. J. **725,** 1563 (2010).

[14] I. Tamborra, F. Hanke, H.-T. Janka, B. Müller, G. G. Raffelt, and A. Marek, Astrophys. J. **792,** 96 (2014).

[15] S. M. Adams, C. S. Kochanek, J. R. Gerke, K. Z. Stanek, and X. Dai, Mon. Not. R. Astron. Soc. **468,** 4968 (2017).

[16] S. M. Adams, C. S. Kochanek, J. R. Gerke, and K. Z. Stanek, Mon. Not. R. Astron. Soc. **469,** 1445 (2017).

[17] S. J. Smartt, Pub. Astron. Soc. Aust. **32,** e016 (2015).

[18] J. R. Gerke, C. S. Kochanek, and K. Z. Stanek, Mon. Not. R. Astron. Soc. **450,** 3289 (2015).

[19] M. Ugliano, H.-T. Janka, A. Marek, and A. Arcones, Astrophys. J. **821,** 69 (2016); **757,** 69 (2012).

[20] T. Sukhbold, T. Ertl, S. E. Woosley, J. M. Brown, and H.-T. Janka, Astrophys. J. **821,** 38 (2016).

[21] E. O'Connor and C. D. Ott, Astrophys. J. **730,** 70 (2011).

[22] A. Burrows, Astrophys. J. **334,** 891 (1988).

[23] C. S. Kochanek, Astrophys. J. **785,** 28 (2014).

[24] E. Lovegrove and S. E. Woosley, Astrophys. J. **769,** 109 (2013).

[25] D. K. Nadyozhin, Astrophys. Space Sci. **69,** 115 (1980).

[26] T.-W. Wong, C. L. Fryer, C. I. Ellinger, G. Rockefeller, and V. Kalogera, arXiv:1401.3032.

[27] W.-Q. Zhang, S. E. Woosley, and A. Heger, Astrophys. J. **679,** 639 (2008).

[28] M. Liebendörfer, O. E. B. Messer, A. Mezzacappa, S. W. Bruenn, C. Y. Cardall, and F. K. Thielemann, Astrophys. J. Suppl. Ser. **150,** 263 (2004).

[29] K. Sumiyoshi, S. Yamada, and H. Suzuki, Astrophys. J. **667,** 382 (2007).

[30] K. Sumiyoshi, S. Yamada, and H. Suzuki, Astrophys. J. **688,** 1176 (2008).

[31] T. Fischer, S. C. Whitehouse, A. Mezzacappa, F. K. Thielemann, and M. Liebendörfer, Astron. Astrophys. **499,** 1 (2009).

[32] K.-C. Pan, M. Liebendörfer, S. M. Couch, and F.-K. Thielemann, Astrophys. J. **857,** 13 (2018).

[33] L. Yang and C. Lunardini, Phys. Rev. D **84,** 063002 (2011).

[34] A. Mirizzi, I. Tamborra, H.-T. Janka, N. Saviano, K. Scholberg, R. Bollig, L. Hüdepohl, and S. Chakraborty, Riv. Nuovo Cimento **39,** 1 (2016).

[35] C. Lunardini, Phys. Rev. Lett. **102,** 231101 (2009).

[36] J. G. Keehn and C. Lunardini, Phys. Rev. D **85,** 043011 (2012).

[37] K. Nakazato, E. Mochida, Y. Niino, and H. Suzuki, Astrophys. J. **804,** 75 (2015).

[38] K. Nakazato, Phys. Rev. D **88,** 083012 (2013).

[39] A. Priya and C. Lunardini, J. Cosmol. Astropart. Phys. 11 (2017) 031.

[40] S. Horiuchi, K. Sumiyoshi, K. Nakamura, T. Fischer, A. Summa, T. Takiwaki, H.-T. Janka, and K. Kotake, Mon. Not. R. Astron. Soc. **475,** 1363 (2018).

[41] K. Møller, A. M. Suliga, I. Tamborra, and P. B. Denton, J. Cosmol. Astropart. Phys. 05 (2018) 066.

[42] I. Tamborra, G. G. Raffelt, F. Hanke, H.-T. Janka, and B. Müller, Phys. Rev. D **90,** 045032 (2014).

[43] I. Tamborra, F. Hanke, B. Müller, H.-T. Janka, and G. G. Raffelt, Phys. Rev. Lett. **111,** 121104 (2013).

[44] T. Lund, A. Wongwathanarat, H.-T. Janka, E. Müller, and G. G. Raffelt, Phys. Rev. D **86,** 105031 (2012).

[45] T. Kuroda, K. Kotake, K. Hayama, and T. Takiwaki, Astrophys. J. **851,** 62 (2017).

[46] T. Lund, A. Marek, C. Lunardini, H.-T. Janka, and G. G. Raffelt, Phys. Rev. D **82,** 063007 (2010).

[47] L. Walk, I. Tamborra, H.-T. Janka, and A. Summa, Phys. Rev. D **98,** 123001 (2018).

[48] L. Walk, I. Tamborra, H.-T. Janka, and A. Summa, Phys. Rev. D **100,** 063018 (2019).

[49] D. Vartanyan, A. Burrows, D. Radice, A. M. Skinner, and J. Dolence, Mon. Not. R. Astron. Soc. **482,** 351 (2019).

[50] A. Burrows, D. Radice, and D. Vartanyan, Mon. Not. R. Astron. Soc. **485,** 3153 (2019).

[51] E. P. O'Connor and S. M. Couch, Astrophys. J. **865,** 81 (2018).

[52] B. Müller, H.-T. Janka, and A. Heger, Astrophys. J. **761,** 72 (2012).

[53] C. D. Ott, E. Abdikamalov, P. Mösta, R. Haas, S. Drasco, E. P. O'Connor, C. Reisswig, C. A. Meakin, and E. Schnetter, Astrophys. J. **768,** 115 (2013).

[54] T. Takiwaki, K. Kotake, and Y. Suwa, Mon. Not. R. Astron. Soc. **461,** L112 (2016).

[55] B. Müller, T. Melson, A. Heger, and H. T. Janka, Mon. Not. R. Astron. Soc. **472,** 491 (2017).

[56] C. D. Ott, L. F. Roberts, A. da Silva Schneider, J. M. Fedrow, R. Haas, and E. Schnetter, Astrophys. J. **855,** L3 (2018).

[57] C. Chan, B. Müller, A. Heger, R. Pakmor, and V. Springel, Astrophys. J. **852,** L19 (2018).

[58] B. Müller, Annu. Rev. Nucl. Part. Sci. **69,** 253 (2019).

[59] H.-T. Janka, T. Melson, and A. Summa, Annu. Rev. Nucl. Part. Sci. **66,** 341 (2016).

[60] T. Kuroda, K. Kotake, T. Takiwaki, and F.-K. Thielemann, Mon. Not. R. Astron. Soc. **477,** L80 (2018).

[61] R. Abbasi et al. (IceCube Collaboration), Astron. Astrophys. **535,** A109 (2011); **563,** C1(E) (2014).

[62] M. Ikeda et al. (Super-Kamiokande Collaboration), Astrophys. J. **669,** 519 (2007).

[63] R. Acciarri et al. (DUNE Collaboration), arXiv: 1512.06148.

[64] S. E. Woosley and A. Heger, Phys. Rep. **442,** 269 (2007).

[65] M. Rampp and H.-T. Janka, Astron. Astrophys. **396,** 361 (2002).

[66] R. Buras, H.-T. Janka, M. Rampp, and K. Kifonidis, Astron. Astrophys. **457,** 281 (2006).

[67] B. Müller, H.-T. Janka, and A. Marek, Astrophys. J. **756,** 84 (2012).

[68] M. A. Skinner, J. C. Dolence, A. Burrows, D. Radice, and D. Vartanyan, Astrophys. J. Suppl. Ser. **241,** 7 (2019).

[69] R. Glas, O. Just, H. T. Janka, and M. Obergaulinger, Astrophys. J. **873,** 45 (2019).

[70] S. M. Couch and E. P. O'Connor, Astrophys. J. **785,** 123 (2014).

[71] A. Kageyama and T. Sato, Geochem. Geophys. Geosyst. **5,** Q09005 (2004).

[72] A. Wongwathanarat, N. J. Hammer, and E. Müller, Astron. Astrophys. **514,** A48 (2010).

[73] A. Marek, H. Dimmelmeier, H.-T. Janka, E. Müller, and R. Buras, Astron. Astrophys. **445,** 273 (2006).

[74] L. Hüdepohl, Neutrinos from the formation, cooling and black hole collapse of neutron stars, Ph.D. thesis, Technische Universität München, 2014.

[75] E. P. O'Connor and S. M. Couch, Astrophys. J. **854,** 63 (2018).

[76] D. Radice, A. Burrows, D. Vartanyan, M. A. Skinner, and J. C. Dolence, Astrophys. J. **850,** 43 (2017).

[77] E. J. Lentz, S. W. Bruenn, W. R. Hix, A. Mezzacappa, O. E. B. Messer, E. Endeve, J. M. Blondin, J. A. Harris, P. Marronetti, and K. N. Yakunin, Astrophys. J. **807,** L31 (2015).

[78] A. d. S. Schneider, E. O'Connor, E. Granqvist, A. Betranhandy, and S. M. Couch, Astrophys. J. **894,** 4 (2020).

[79] T. Melson, D. Kresse, and H.-T. Janka, Astrophys. J. **891,** 27 (2020).

[80] D. Radice, C. D. Ott, E. Abdikamalov, S. M. Couch, R. Haas, and E. Schnetter, Astrophys. J. **820,** 76 (2016).

[81] H. Nagakura, A. Burrows, D. Radice, and D. Vartanyan, Mon. Not. R. Astron. Soc. **490,** 4622 (2019).

[82] J. M. Lattimer and F. D. Swesty, Nucl. Phys. **A535,** 331 (1991).

[83] M. Oertel, M. Hempel, T. Klähn, and S. Typel, Rev. Mod. Phys. **89,** 015007 (2017).

[84] A. W. Steiner, M. Hempel, and T. Fischer, Astrophys. J. **774,** 17 (2013).

[85] E. Müller, H. T. Janka, and A. Wongwathanarat, Astron. Astrophys. **537,** A63 (2012).

[86] T. Yamasaki and T. Foglizzo, Astrophys. J. **679,** 607 (2008).

[87] J. M. Blondin and S. Shaw, Astrophys. J. **656,** 366 (2007).

[88] D. Vartanyan, A. Burrows, and D. Radice, Mon. Not. R. Astron. Soc. **489,** 2227 (2019).

[89] A. Marek, H.-T. Janka, and E. Müller, Astron. Astrophys. **496,** 475 (2009).

[90] T. Takiwaki and K. Kotake, Mon. Not. R. Astron. Soc. **475,** L91 (2018).

[91] See Supplemental Material at http://link.aps.org/supplemental/10.1103/PhysRevD.101.123013 for Time evolution of the electron antineutrino luminosity normalized to its average $[(L_{\bar{\nu}_e} - \langle L_{\bar{\nu}_e} \rangle)/\langle L_{\bar{\nu}_e} \rangle]$ on a Mollweide map of the progenitor's emission surface for the 40 $M_\odot$ and 75 $M_\odot$ BH-forming models.

[92] F. Hanke, B. Müller, A. Wongwathanarat, A. Marek, and H.-T. Janka, Astrophys. J. **770,** 66 (2013).

[93] R. Fernàndez, Mon. Not. R. Astron. Soc. **452,** 2071 (2015).

[94] A. Summa, H. T. Janka, T. Melson, and A. Marek, Astrophys. J. **852,** 28 (2018).

[95] T. Kuroda, K. Kotake, and T. Takiwaki, Astrophys. J. **829,** L14 (2016).

[96] T. Foglizzo, P. Galletti, L. Scheck, and H.-T. Janka, Astrophys. J. **654,** 1006 (2007).

[97] F. Hanke, A. Marek, B. Müller, and H.-T. Janka, Astrophys. J. **755,** 138 (2012).

[98] J. Guilet and T. Foglizzo, Mon. Not. R. Astron. Soc. **421,** 546 (2012).

[99] R. Fernández, B. Müller, T. Foglizzo, and H.-T. Janka, Mon. Not. R. Astron. Soc. **440,** 2763 (2014).

[100] N. Ohnishi, K. Kotake, and S. Yamada, Astrophys. J. **641,** 1018 (2006).

[101] R. Glas, H.-T. Janka, T. Melson, G. Stockinger, and O. Just, Astrophys. J. **881,** 36 (2019).

[102] H. Nagakura, A. Burrows, D. Radice, and D. Vartanyan, Mon. Not. R. Astron. Soc. **492,** 5764 (2020).

[103] L. Wolfenstein, Phys. Rev. D **17,** 2369 (1978).

[104] S. Horiuchi and J. P. Kneller, J. Phys. G **45,** 043002 (2018).

[105] J. P. Kneller and M. de los Reyes, J. Phys. G **44,** 084008 (2017).

[106] K. M. Patton, J. P. Kneller, and G. C. McLaughlin, Phys. Rev. D **91,** 025001 (2015).

[107] S. Chakraborty, R. Hansen, I. Izaguirre, and G. G. Raffelt, Nucl. Phys. **B908,** 366 (2016).

[108] I. Izaguirre, G. G. Raffelt, and I. Tamborra, Phys. Rev. Lett. **118,** 021101 (2017).

[109] R. F. Sawyer, Phys. Rev. D **72,** 045003 (2005).

[110] M. T. Keil, G. G. Raffelt, and H.-T. Janka, Astrophys. J. **590,** 971 (2003).

[111] A. Strumia and F. Vissani, Phys. Lett. B **564,** 42 (2003).

[112] Y. Fukuda et al. (Super-Kamiokande Collaboration), Nucl. Instrum. Methods Phys. Res., Sect. A **501,** 418 (2003).

[113] S. Seadrow, A. Burrows, D. Vartanyan, D. Radice, and M. A. Skinner, Mon. Not. R. Astron. Soc. **480,** 4710 (2018).

[114] T. Foglizzo, L. Scheck, and H. T. Janka, Astrophys. J. **652,** 1436 (2006).

[115] R. Kazeroni, J. Guilet, and T. Foglizzo, Mon. Not. R. Astron. Soc. **456,** 126 (2016).

[116] V. Srivastava, S. Ballmer, D. A. Brown, C. Afle, A. Burrows, D. Radice, and D. Vartanyan, Phys. Rev. D **100,** 043026 (2019).

[117] H. Andresen, E. Müller, H.-T. Janka, A. Summa, K. Gill, and M. Zanolin, Mon. Not. R. Astron. Soc. **486,** 2238 (2019).

[118] J. R. Westernacher-Schneider, E. O'Connor, E. O'Sullivan, I. Tamborra, M.-R. Wu, S. M. Couch, and F. Malmenbeck, Phys. Rev. D **100,** 123009 (2019).